Visual investigation of the gas/liquid interface in annular pipe flows

MSc Thesis

DELFT UNIVERSITY OF TECHNOLOGY
FACULTY OF APPLIED SCIENCES
DEPARTMENT OF MULTI-SCALE PHYSICS

Starting date: 31 august 2009
Defence date: 20 august 2010

Author:
Rudi KALTER
Studentnumber: 1174096

Supervisor:
Dr. Eng. L.M. PORTELA

Reviewers:
Prof. Dr. Ir. R.A.W.M. Henkes
Dr. M.J. Tummers
Ir. G.P.H.A. de Oliveira

Abstract

Annular flows are encountered in wet gas-wells. When gas is extracted from the well, a small amount of liquid is dragged up as well. The combination of high gas velocity and low liquid flow rate causes an annular flow to exist. As the gas well is employed for longer times, the pressure in the gas well decreases. Due to this decrease in gas pressure, the gas velocity decreases and at a certain point the gas is unable to drag the liquid up. When this happens, the liquid will fall back and this is called liquid loading. Liquid loading is a major problem in the exploitation of gas wells.

In this investigation, the gas/liquid interface in annular flow in a horizontal pipe was examined, using a 12.5 meters long and 5 cm in diameter acrylic pipe. The flow was visualised with a high speed camera with a high resolution. To be able to make pictures of the gas/liquid interface a hole was made in the pipe through which the interface was visualised. The hole disturbs the flow, but the part of the flow that was filmed is not disturbed. With the use of the high speed camera, different phenomena occurring in the gas/liquid interface were examined.

Previous to the annular flow study, in order to get experience with the visual techniques and the flow loop, a preliminary investigation was made on gas/liquid stratified flow. This investigation showed that it is possible to obtain good qualitative and quantitative information on the droplet entrainment and ligament formation at the liquid surface; this shows the potential of the technique for future detailed studies.

The gas/liquid interface in annular flows can be best described as a rippled surface, interchanged with roll waves. In this work, both ripple waves and roll waves are investigated. From visual inspection, data is presented on the ripple-wave orientation in the flow, the ripple-wave velocity and the sizes of the ripples. The roll waves were examined by visual inspection and by an automated process. Data is presented on the macro properties: roll-wave frequency, velocity and length.

Besides these macro properties, the structure of the roll wave itself are examined. Observations show that roll waves contain large coherent structures, with droplets and ligaments travelling above the liquid film. Estimates made of the amount of liquid entrained just above the roll wave showed that this is a significant fraction of the total amount of liquid entrained. The liquid mass-fraction in the region of the roll wave is estimated to be 10, indicating that in this region two-way coupling effects between the gas end the entrained liquid must play a role.

The maximum droplet diameters above the roll waves were compared to droplet diameters predicted by the Turner criterion. The Turner criterion is a standard way to predict

the onset of liquid loading in industrial applications. The maximum droplet diameters found in this work give a good comparison with the droplet diameters predicted by the Turner criterion. This gives an indication why the Turner criterion predicts the onset of liquid loading correctly: it is associated with the droplets above the roll waves. In a previous study, van 't Westende [32] measured the droplets in the gas core, which are significantly smaller, and not consistent with the Turner criterion.

The maximum droplet diameters are found in the region close to the gas/liquid interface above the roll waves. This suggests that the onset of liquid loading is initiated at the gas/liquid interface.

List of symbols

Roman Symbols

Symbol	Description	Units
$A_\perp$	Frontal area	$[m^2]$
A_{gas}	Frontal area of the gas	$[m^2]$
A_{liquid}	Frontal area of the liquid	$[m^2]$
A_{pipe}	Frontal area of the pipe	$[m^2]$
C_w	Constant depending on viscosity group	$[-]$
C_d	Drag coefficient	$[-]$
D	Pipe diameter	$[m]$
E	Droplet entrainment	$[m^3]$
E_l	Entrainment per unit roll-wave length	$[m^3/m]$
E_t	Entrainment per unit time	$[m^3/s]$
F_d	Drag force	$[N]$
F_g	Gravitational force	$[N]$
L_w	Roll-wave length	$[m]$
R	Spatial resolution	$[m/pixel]$
$\dot{V}_g$	Volumetric gas flow rate	$[m^3/s]$
Z_{eq}	Development length	$[m]$
a_1	Projection of a point on a picture	$[-]$
b	Mutual distances between two cameras	$[m]$
$d_{dr,max}$	Maximum droplet diameter	$[m]$
g	Gravitational acceleration	$[m/s^2]$
f	Focal length	$[m]$
f_w	Roll-wave frequency	$[s^{-1}]$
h_1	Elevation of camera above a horizontal plane	$[m]$
h_2	Elevation of a point above a reference plane	$[m]$
$\dot{m}_g$	Gas mass flow rate	$[kg/s]$
$\dot{m}_l$	Liquid mass flow rate	$[kg/s]$
n	Geometric centre of a picture	$[-]$
p	Parallax	$[m]$
r	Radius	$[m]$
$u_{dr,t,max}$	Terminal free-fall velocity for the largest drop	$[m/s]$
u_{drop}	Droplet velocity	$[m/s]$
u_g	Gas velocity	$[m/s]$
u_l	Liquid velocity	$[m/s]$
u_{sg}	Superficial gas velocity	$[m/s]$
u_{sl}	Superficial liquid velocity	$[m/s]$
u_w	Roll-wave velocity	$[m/s]$

Greek Symbols

Symbol	Description	Units
$\alpha_{dr,wave}$	Void fraction due to a roll wave	$[m^3/m^3]$
Δt	Time difference	$[s]$
Δpx	Difference in number of pixels	$[-]$
ε	Energy dissipation rate	$[m^2/s^3]$
μ_g	Dynamic gas viscosity	$[kg/ms]$
μ_l	Dynamic liquid viscosity	$[kg/ms]$
ρ	Density	$[kg/m^3]$
ρ_g	Gas density	$[kg/m^3]$
ρ_l	Liquid density	$[kg/m^3]$
$\Delta\rho$	Density difference	$[kg/m^3]$
σ	Surface tension	$[N/m]$
τ	External stresses	$[N]$

Abbreviations

Abbreviation	Description
CCD	Charge Coupled Device
CMOS	Complementary Metal Oxide Semiconductor
DOF	Depth of Field
fps	Frames per Second
i.d.	In Diameter
PDA	Phase Doppler Anemometry
ULLN	Upper Limit Log Normal

Dimensionless groups

Symbol	Description	
INT	Intermittency	$\frac{f_w L_w}{v_w}$
Re_G	Gas Reynolds number	$\frac{\rho_g u_g D}{\mu_g}$
Re_L	Liquid Reynolds number	$\frac{\rho_g u_g D}{\mu_g}$
We	Weber number	$\frac{\rho u^2 d_{dr}}{\sigma}$
We_{crit}	Critical Weber number	$\frac{\rho_g u_{dr,t,max}^2 d_{dr,max}}{\sigma}$
We_m	Modified Weber number	$\frac{\rho_g u_{sg}^2 D}{\sigma}$

Contents

Chapter 1

Introduction

1.1 Motivation

The subject of multiphase flows deal with the hydrodynamics of two or more immiscible phases of matter (gas, liquid or solid). Multiphase flows are commonly encountered in both nature and technology, like in rain, sand storms or fuel injection in an engine.

In the context of this thesis, gas/liquid pipe flows are involved. These kind of flows are commonly present in industrial applications like the exploitation of gas wells. Gas wells are underground reservoirs that contain gas-phase hydrocarbons. When gas is produced from the gas wells, the pressure in the well decreases and consequently the gas flow rate decreases.

In wet gas wells, a small amount of liquid is present in the reservoir, this is typically around 0.003 % of the reservoir volume, Kemp [20]. For a high gas flow rate, liquid is transported to the surface as well in the form of annular flow. The main goal of this thesis is to get a fundamental understanding of the processes at the gas/liquid interface in annular flows.

When the pressure in the gas well decreases, the gas phase does not supply enough energy to the liquid to drag it upward. The liquid will flow back and accumulate in the bottom of the pipe, this is called liquid loading. Liquid loading is a major problem in the exploitation of wet gas wells, since the liquid accumulates at the well bore. This affects the production of the gas well significantly, and in low pressure wells the liquid loading might even kill the well. In this project horizontal flows are considered, so no liquid loading is visualised. One of the aims is to get an understanding of the processes when the gas glow is not able to drag the liquid along.

1.2 Flow regimes

In gas/liquid pipe flows different flow-patterns are known, depending on the orientation of the pipe and on the flow rates of the gas and the liquid. In vertical pipe flows, the following flow patterns are encountered when the gas flow rate is increased and the liquid flow rate is kept constant, these flow patterns are shown in Figure 1.1:

- Bubbly flow: Gas bubbles move upwards through the liquid phase, driven by buoyancy.

- Slug flow: Large Taylor bubbles move upwards through the liquid phase. Between the Taylor bubbles, also smaller bubbles are entrained.

- Churn flow: Unstable flow, of an oscillatory nature, characterised by oscillatory up and down motions of the liquid.

- Annular flow: The gas phase is the continuous phase, liquid is present as a thin liquid film along the pipe wall and as droplets in the gas core.
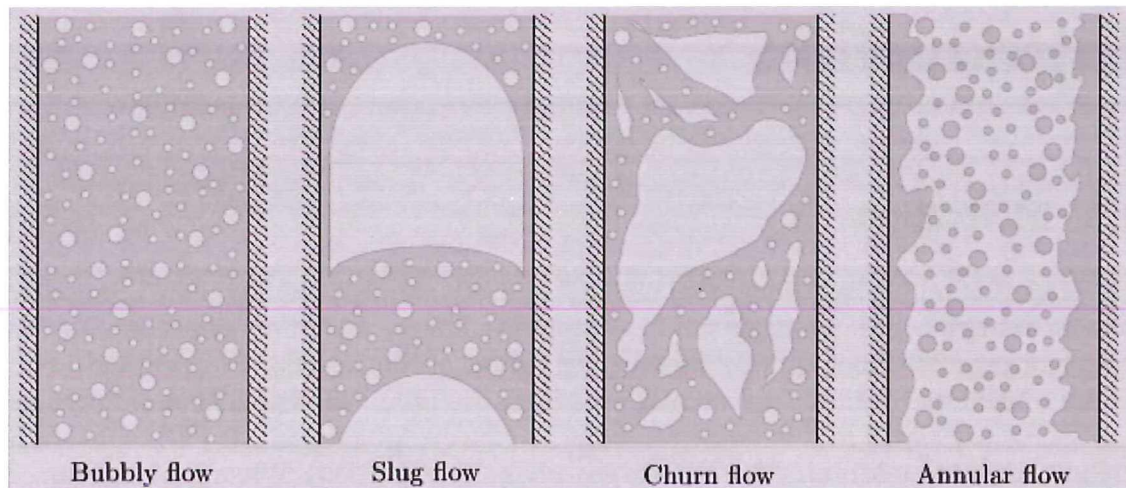

Figure 1.1: Flow patterns for a vertical upward gas/liquid pipe-flow, van't Westende [32]

For a horizontal pipe, the gravitational force breaks the axi-symmetry, the heavier phase is more likely to be found at the bottom of the pipe. When keeping the liquid flow rate constant and by increasing the gas flow rate, the different flow patterns are:

- Bubbly flow: Gas bubbles move through the liquid phase. Due to the buoyancy the gas bubbles are found at the top of the pipe.

- Slug flow: Large slugs of gas, also known as Benjamin bubbles move through the continuous liquid phase. Between the bubbles, smaller bubbles are present.

- Stratified flow: Liquid and gas flow separately through the pipe, in the gas phase, liquid droplets can be entrained.

- Annular flow: The gas phase is the continuous phase and liquid flows as a thin layer along the pipe circumference. Due to gravitational settling the liquid layer at the bottom of the pipe will be thicker than at the top.

In Figure 1.2 the different flow-patterns for horizontal pipe-flow are illustrated with increasing gas flow-rate.

1.3   Separated flows

The flow regimes mentioned in section 1.2 can roughly be separated in two classes: Dispersed flows, where gas is entrained in the continuous liquid phase and separated flows,
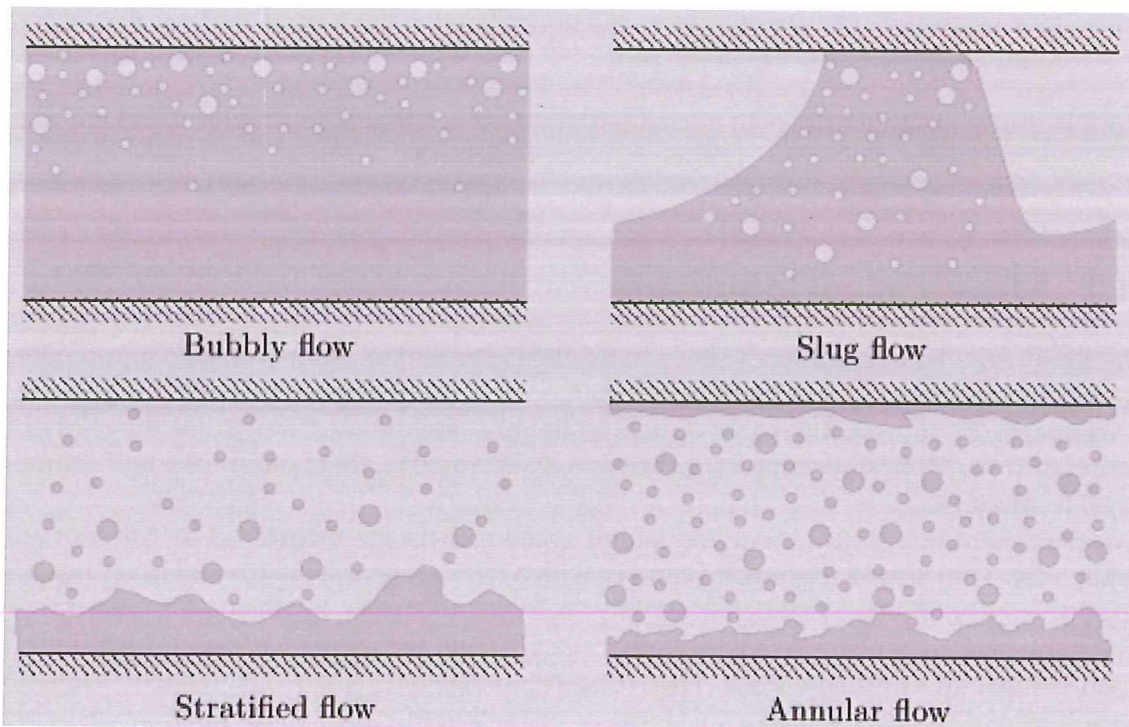
Figure 1.2: Flow patterns for a horizontal gas/liquid pipe-flow, van't Westende [32]

where the gas and liquid phase live next to each other as separated continuous phases. The separated flows considered here are stratified and annular flows in horizontal pipes. In stratified and annular flow part of the liquid is present as a liquid film, separated from the continuous gas phase. Another part of the liquid is dispersed as droplets in the gas core, so annular flow can be regarded as a combination of dispersed and separated flow. For low gas velocities and a relatively high liquid flow rate, stratified flow is present. The liquid phase occupies the bottom of the pipe, due to the gravitational force. The gas phase flows over the liquid phase. Due to shear stresses between the gas and liquid phase, disturbances occur and these disturbances cause a part of the liquid to atomise into the gas phase.

When the gas velocity is increased, annular flow will occur. Here the whole circumference of the pipe will be covered with a liquid film and the gas phase will be present in the core. The shear stresses between the phases will, again, cause liquid to atomise into the gas phase.

In a horizontal flow the liquid will always be drawn to the bottom of the pipe due to the gravitational attraction, so for the annular flow to remain there must be a mechanism that draws the liquid to the top of the pipe. Van 't Westende [32] states that in literature three mechanisms are proposed to explain why the liquid is drawn or pushed to the top of the pipe:

- Secondary flow in the gas core, a drag is exerted on the film due to the non uniform surface roughness or due to the non uniform droplet concentration.

- Wave pumping/spreading, which leads the roll waves and liquid to climb up the walls.

- Net entrainment of droplets from the liquid layer at the bottom and net deposition of the droplets to the top of the pipe.

In this thesis, stratified flows in horizontal pipes are examined in chapter 4 and annular flows in horizontal pipes are examined in chapters 5 to 8.

1.4   Measurement techniques

In literature, a lot of attention is given to the measurement techniques in gas/liquid pipe-flow. An overview of techniques to determine the drop sizes in annular flow is given by Azzopardi [5], he concludes that optical techniques are the most suited for the study of annular flow. Optical techniques mentioned by Azzopardi are photography and diffraction techniques.
Measurement techniques involving a high speed camera are mentioned by Marmottant et.al. [23]. They used a high speed camera with a frame rate of 4,500 fps and a continuous backward illumination through a diffusive screen to visualise ligaments torn of a spray. Wohono et.al. [33] also use a high speed visualisation technique with backward illumination through a diffusive sheet. They use a frame rate of 2,000 to 3,000 fps with a spatial resolution of 66 μm/pixel on a CCD sensor consisting of 1,280 x 1,024 pixels to visualise the break up of an annular sheet.
Ohba and Nagae [25] use a pigment luminance technique to visualise annular flow in a 2.9 cm i.d. pipe. They dissolve particles of 5 μm to a volume concentration of 0.025 %. With a high speed camera, pictures are taken of the flow and the film thickness is correlated to the brightness of the picture.

1.5   Literature review

A lot of research has been done on the topic of annular gas/liquid flows. Most of the references deal with either the droplet entrainment in the gas core or with the behaviour of the liquid film.
Hay et al. [13] and van 't Westende [32] used techniques with which they can extract the liquid film and collect data on the droplets in the gas core. These techniques give results on the total droplet entrainment in the gas core. In chapter 8 data from the current work is compared to the data provided by van 't Westende, a good comparison with the data from Hay et al. is not possible since they use vertical annular flows.
Asali et al. [2] and Belt [6] report measurement results on the liquid film thickness using conductance of the liquid. The results from Belt are used in chapter 8 to compare the liquid film thicknesses with the roll-wave height.
A small amount of work has been done on the actual gas/liquid interface in horizontal annular flow. Hall-Taylor et al. [11] come with an overview of the liquid surface in annular pipe flows. Their view is given in Figure 5.1. The measurements from Hall-Taylor et al. are done by use of cine-film methods. The pictures are not very detailed, but give an overview of the amount of roll waves passing by in a certain amount of time, the results are for vertical annular flows. Ohba et al. [25] and Paras et al. [26] also use film techniques to visualise the flows. Ohba et al. do this for vertical annular flows and Paras et al. for horizontal flows. The results found in the present work are compared to Paras et al. in chapter 7.

Recently, Schubring et al. [29] published a paper in which they study disturbance waves in vertical annular flow with high speed video. In their work, they report on roll-wave velocities, frequencies and sizes. The work in this thesis can contribute to a further, better understanding of the roll waves in horizontal flow using more or less the same technique as Schubring, but zooming in on the smaller structures in the flow.

1.6   This work

The objective of this work is to visualise and analyse the entrainment mechanisms in gas/liquid annular pipe-flow. This is done using a 12.5 m long and 5 cm in diameter acrylic pipe and a high speed camera. From the literature it is known that droplets in the core of an annular flow can vary in size from 10 μm up to millimetres, while the instabilities in the flow have sizes of the order of the pipe diameter. From this it is desired that the camera can capture both the large structures and the small structures.

This study is performed to give an accurate representation of the atomisation process. From this representation an accurate description of the atomisation-pdf can be formulated, which can be used as input for simulations on annular flow. This was given as one of the recommendations by van 't Westende [32].

Furthermore, the topology of the surface of the liquid film can be captured with a high resolution. With this a better understanding of the surface roughness due to the liquid film can be given.

The results from this work can contribute to a better understanding of the physical behaviour of the gas/liquid interface in annular flows. Since most of the work so far is done on either the droplet entrainment in the gas core or the behaviour of the liquid film thickness, this can contribute to a more complete understanding of the annular flow. The goal is to zoom into the smallest structures in the flow, with a higher spatial resolution than Ohba et al. [25] or Schubring et al. [29]. With this a better description of the roll waves can be given.

This project is performed as a graduation project for the Master programme Applied Physics at Delft University of Technology. The work was done at the Multi Scale Physics department of the faculty of Applied Sciences.

1.7   Outline

This thesis starts with an introduction to droplet atomisation. Different experimental and theoretical descriptions are given. In chapter 3, the set-up for the experiments in this thesis is described. In chapter 4, the results of a preliminary study on stratified flow in a horizontal pipe are given. The study on stratified flows was done to get a better feeling of the experimental set-up and to investigate some possibilities for future. Chapter 5 gives a short introduction to the phenomena in annular flows, before going into the details of ripple-wave patterns in chapter 6, and roll-wave patterns in chapter 7. In chapter 8, the main work on the interpretation of the disturbance waves is presented. Conclusions and recommendations are given in chapter 9.

Chapter 2

Droplet atomisation

2.1 Droplet entrainment

In stratified wavy and annular flows, droplet entrainment occurs. This means that in the gas core in the pipe, droplets move with a velocity comparable to the gas velocity. In the literature references are found on the topic of droplet entrainment, predominantly with data on equilibrium situations. The equilibrium amount of entrainment results from a balance between the atomisation and deposition of droplets from and onto the film. The total amount of entrainment is reported from experiments by e.g. Ishii et al. [19] and Sawant et al. [28].

Van 't Westende [32] suggested that a good physical understanding of the entrainment rate comes from a good understanding of the wavy structure of the liquid film. Entrainment only occurs when roll waves are present in the flow. Azzopardi [5] created a smooth liquid surface and injected little quantities of liquid to induce roll waves. When no roll waves were present, no entrainment was measured.

Belt [6] used a non-intrusive film thickness probe to reconstruct the interface with a high resolution in time and a modest space resolution. This conductance probe lacks the spatial resolution to distinguish the smaller structures on the roll waves, which are responsible for the entrainment of droplets.

2.2 Entrainment mechanisms

Ishii et al. [19] gave an overview of mechanisms which are possible for atomisation in annular flow; these are summarised in figure 2.1. The same mechanisms were confirmed by van't Westende [32] and Hewitt et al. [15]. Van 't Westende [32] suggested that from the given break up mechanisms, two major contributors can be distinguished: Bag break up and ligament break up.

Bag break up is comparable with the wave undercut mechanism from figure 2.1. With bag break up the liquid film is undercut by the gas flow, forming an open ended bubble with a thick filament rim. Both the bubble and the filament rim break up in droplets. This kind of mechanism occurs at a lower gas and liquid flow rate.

Ligament break up is comparable to the roll-wave type of break up. This type of mechanism becomes important at higher flow rates. In ligament forming, the crest of the roll waves is elongated and thin ligaments are torn from the film, breaking up in droplets, Azzopardi [5] and Marmottant et al. [23].

The mechanisms causing the droplets to entrain into the gas core are essentially of a wavy

nature. These waves are caused by Kelvin-Helmholtz instabilities in the flow. Wood-mansee et al. [34] state that the destabilising force is the pressure variation caused by the compression of the air streamlines at the crests of wavelets. A description of a Kelvin-Helmholtz analysis is given in chapter 6 of the book of Hewitt et al. [15].

Han et al. [12] have been working on numerical simulation of entrainment in annular flow. The details of the entrainment mechanisms are well described by their numerical simulation work. In the work of Han et al. [12] two main entrainment mechanisms are proposed. At a high gas velocity the individual waves continue to develop and deform until the crest is sheared off, this is comparable to the roll-wave mechanism from figure 2.1. The second mechanism, at a lower gas velocity is referred to as wave coalescence, which is a new phenomenon compared to the mechanisms proposed by Ishii et al. [19].
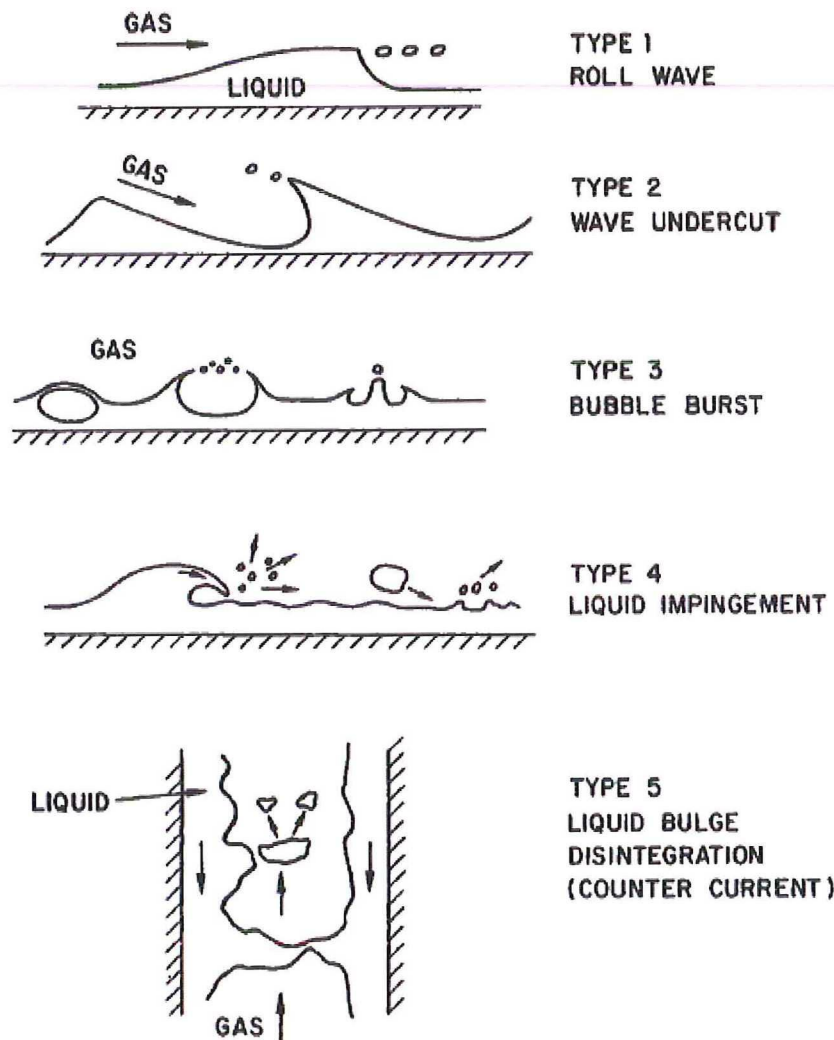
Figure 2.1: Different droplet entrainment mechanisms in annular and stratified wavy pipe flows, Ishii et al. [19]

2.3   Droplet size distribution

An important feature in droplet entrainment in annular flow is the size of the droplets in the gas core. A study on the drop sizes was done by Hay et al. [14]; in this study the liquid film was removed from the flow and the droplets moving through the gas core were recorded using a high resolution CCD camera. With this technique, droplets of 50 μm in diameter and larger can be observed. Hay et al. [13] also did work on the size distribution of the droplets in annular pipe flow. They compared their data with two known correlations for the drop size distribution. One is the Rosin-Rammler distribution, proposed by Rosin and Rammler [27] which was originally designed to describe the mass distribution of coal dust obtained from sieving. The other distribution is the "upper limit log normal" distribution, suggested by Mugele et al. [24]. The "ULLN" distribution gives in general a better fit to the data. The data and distributions are given in figure 2.2.
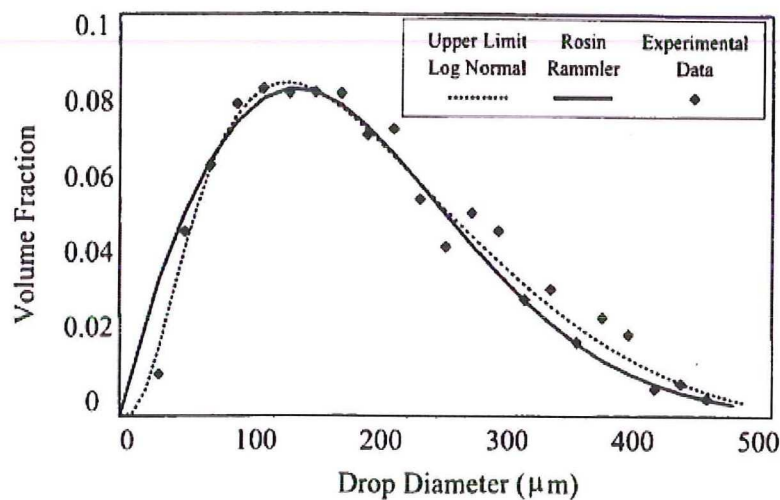

Figure 2.2: Test of Rosin-Rammler and upper limit log normal distributions against data of Hay et al. [13]. Picture from Azzopardi [5].

Recently, van 't Westende [32] did measurements on the drop size distribution in vertical annular flow. His results show that there are two exponential tails in the distribution, probably the superposition of two droplet size distributions. For the higher gas velocities it seems that the droplets close to the gas liquid interface are smaller than the droplets in the centre of the pipe. Droplets larger than approximately 600 μm are hardly measured, since they are deformed, van 't Westende could only measure spherical droplets. Van 't Westende estimates that droplets larger than 600 μm are only 0.1 % of all the droplets so the drop size distribution is very noisy for $d_{dr} > 600$ μm. The drop size distributions of van 't Westende are shown in figure 2.3.

Turner Criterion

For the prediction of the flow reversal point, the analysis by Turner at al. [30] is widely used. The onset of liquid loading is related to the ability of the gas stream to keep the
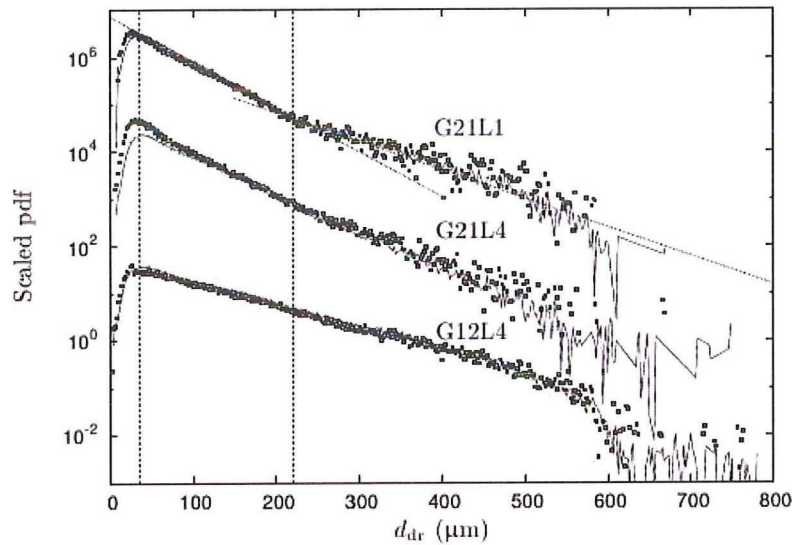
Figure 2.3: Drop size distributions measured by van 't Westende [32] for vertical annular and churn flows. G21L1 and G21L4 are annular flows and G12L4 is churn-annular flow. Measurements were done at the centre of the pipe (solid line) and at 3.5 cm from the centre (symbols).

largest droplet pending. To estimate the sizes of the largest droplets, present in turbulent flow, Turner et al. used an analysis involving a critical Weber number. This critical Weber number is defined as:

$$We_{crit} = \frac{\rho_g u_{dr,t,max}^2 d_{dr,max}}{\sigma} = 30 \tag{2.1}$$

σ is the surface tension and $u_{dr,t,max}$ is the terminal free-fall velocity for the largest drop. The predicted flow reversal point occurs when $u_{sg} = u_{dr,t,max}$.
The assumption is made that the droplets are still spherical, so a drag coefficient of 0.44 is appropriate. This results in the following correlation for the terminal free-fall velocity:

$$u_{dr,t,max} = \left(\frac{90.9 g \sigma (\rho_l - \rho_g)}{\rho_g^2}\right)^{0.25} \tag{2.2}$$

Using this analysis, a maximum droplet diameter of 8.5 mm is calculated, with a corresponding free-fall velocity of 14.5 m/s. Maximum droplet diameters, reported in literature, for air water systems are around 2 mm (van 't Westende [32]).

Maximum drop size in turbulent flow

For the determination of the maximum stable droplet sizes in turbulent flow, the analysis by Kocamustafaogullari et al. [21] is followed. Two forces keep droplets together, external stresses, τ, and the surface stress $\sigma/(d/2)$, where σ is the surface tension and d is the droplet diameter. In highly turbulent flows ($Re_{sg} \gg 1$) viscous forces are negligible. The external stress, τ, can then be expressed as a kinetic energy difference around the droplet. In this case, a change of eddy velocities over the length of a droplet are considered. This

gives a critical Weber number relation:

$$We_{crit} = \frac{\rho_g u_{r,max}^2 d_{dr,max}}{2\sigma} \tag{2.3}$$

$u_{r,max}$ is the local relative velocity with which fluid will flow around a particle. This velocity is related to the energy dissipation rate per unit mass, ε, by:

$$u_{r,max} \sim \left(\varepsilon d_{dr,max} \frac{\rho_l}{\rho_g}\right)^{1/3} \left(\frac{\Delta\rho}{\rho_l}\right)^{1/2} \tag{2.4}$$

The energy dissipation rate depends on the interfacial shear and is approximated by Lopes and Dukler [22]. With this approximation in mind, a correlation for the interfacial shear is given by Ishii et al. [19] and when these correlations are taken into account, the following correlation for the maximum droplet diameter follows:

$$d_{max} = 2.609 DC_w^{-4/15} We_m^{-3/5} \left(\frac{Re_{sg}^4}{Re_{sl}}\right)^{1/15} \left(\frac{\rho_g \; \mu_g}{\rho_l \; \mu_l}\right)^{4/15} \tag{2.5}$$

Here, C_w is a constant, depending on a viscosity group, D is the diameter of the pipe, Re_{sl} and Re_{sg} are the superficial liquid and gas Reynolds numbers, μ_l and μ_g are the liquid and gas viscosities and ρ_l and ρ_g are the liquid and gas densities. We_m is a modified Weber number, defined as $We_m = \rho_g D u_{sg}^2/\sigma$.

When values for the superficial liquid velocities of 1 to 20 cm/s and superficial gas velocities of 20 to 40 m/s are filled in for gas/liquid flows in a 5 cm i.d. pipe, it is seen that maximum droplet diameters range approximately from one to two mm. This is visualised in figures 2.4 and 2.5. As seen from figure 2.3, droplet of this size are not observed in the core of the pipe.
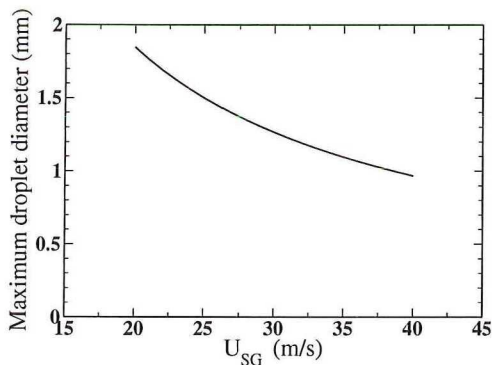
Figure 2.4: Maximum droplet diameter, depending on the superficial gas velocity when the superficial liquid velocity is 5 cm/s. This curve follows from equation 2.5.
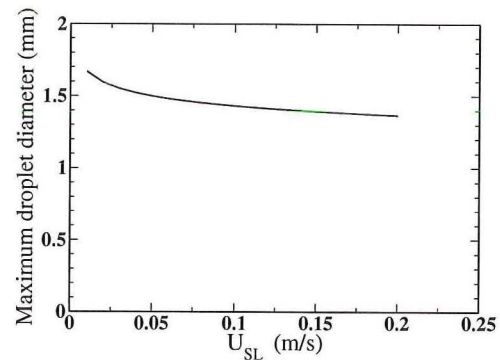
Figure 2.5: Maximum droplet diameter, depending on the superficial liquid velocity when the superficial gas velocity is 25 m/s. This curve follows from equation 2.5.
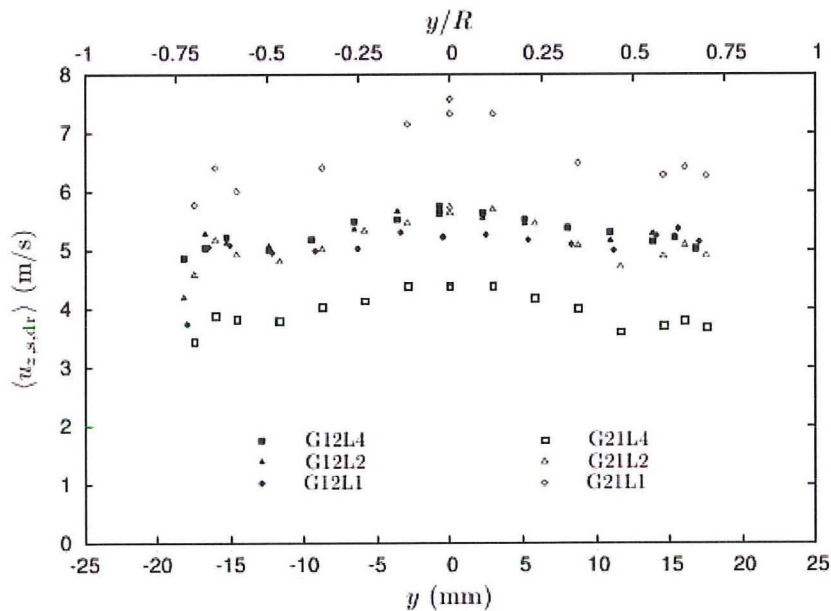
2.4   Droplet velocity

In the measurement of the droplet velocity, Azzopardi [5] mentions two reports on simultaneous drop size and velocity measurement. One is by Azzopardi and Teixeira [4]

and the other by Fore et al. [9], [10]. The results from these groups show similar trends. The mean drop velocities are around 20% lower than the gas velocity, but a wide range of velocities is apparent. This is explained by the fact that a range of droplet sizes is present. Smaller droplets are easier affected by the gas turbulence so, on average, they have a larger velocity but the spread in the velocity is larger too. Larger droplets will show a narrower range of velocities because they are less susceptible to turbulence. The upper limit for the droplet velocity is the gas velocity.

Andreussi et al. [1] reports on lateral or transverse droplet velocities. The results show that the lateral velocity of the droplets hardly changes over their lifetime and are independent of drop size and ejection angle from the liquid film.

In the recent work by van 't Westende [32], also the droplet velocity was measured. From van 't Westende especially the data on droplet slip velocities is of interest. The droplet slip velocity is defined as $\langle u_{z,s,dr} \rangle = \langle u_{z,g} \rangle - \bar{u}_{z,dr}$ and results from van 't Westende are given in figure 2.6. It is seen that for the annular flow regimes, the slip velocity grows with increasing liquid flow rate. With a superficial liquid velocity of 4 cm/s the slip velocity is around 4 m/s, so the droplet velocity is around 80 % of the gas velocity, but with a superficial liquid velocity of 1 cm/s the droplet velocity drops to only 60 % of the gas velocity.

Figure 2.6: Droplet slip velocity in a cross section of the pipe, y=0 is in the centre of the pipe (van 't Westende [32]). The codes GaLb mean, $u_{sg} = a\,m/s$ and $u_{sl} = b\,cm/s$.

Chapter 3

Experimental setup

3.1 Flow loop

3.1.1 Basic flow loop

During the project, the flow loop described by Belt [6] and van 't Westende [32] was used. The flow loop consists of a 12.5 m acrylic pipe with an inner diameter of 50 mm. The pipe is mounted on a rig which can be inclined to any angle between the horizontal and the vertical. The flow loop is shown in figure 3.1

At the bottom of the pipe, dry air, supplied with a compressor is blown into the pipe at near atmospheric conditions. At 1.13 m from the air inlet a water film is created along the circumference of the pipe, using a porous wall. The flow rates of water and air are regulated with rotameters, which were calibrated by Hidma [16] and van Bueren [7]. The rotameters have an accuracy of 2% for the gas flow and 4% for the liquid flow.

3.1.2 Adjustments

The pipe consists of segments which have been connected by flanges. In order to analyse the characteristics of atomisation in annular flow, a hole was made in one of the segments of the pipe. This segment can be placed at different distances from the water inlet. Through this hole, a camera can make images of the flow inside the pipe without disturbance of the view by the flow on the pipe. The pipe has to stay air and water tight, for this a small piece of tube is placed inside the hole which is sealed with an o-ring. This small piece of tube pinches through the pipe.

The piece of tube affects the flow, since it pierces through the annular sheet at the top of the pipe. In order to see to what extend the hole in the pipe disturbs the flow, the small tube is made movable in the pipe. With this the influence of this tube in the pipe can be tested at different depths. From observations it is seen that the hole in the pipe only affects the flow up stream of the hole. This means that the flow analysed is not affected by the hole in the pipe. A schematic view of the hole in the pipe is given in figure 3.2.
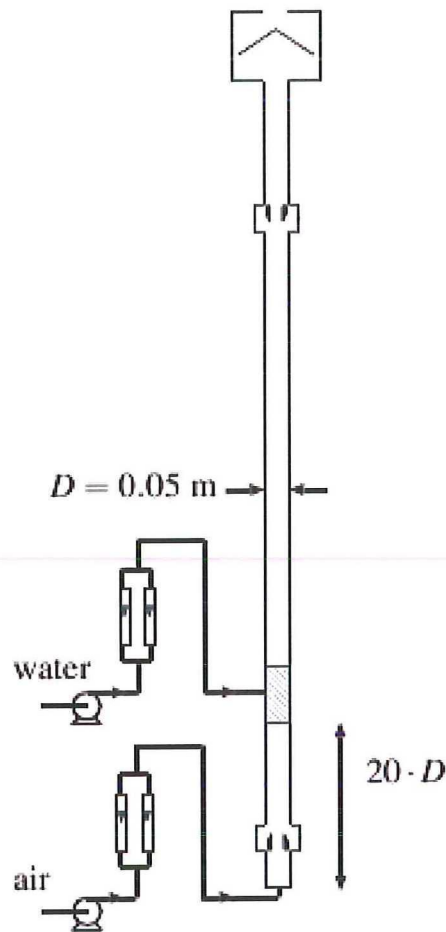
Figure 3.1: Experimental setup of the flow loop in the vertical position. The pipe is 12.5 m long and has a 50 mm inner diameter. A water injection system is situated at 1.13 m from the gas inlet. The angle of the pipe with the horizontal can vary from zero to ninety degrees.

3.2   Olympus i-Speed 2 camera

3.2.1   Camera

For image processing a high speed Olympus i-speed 2 camera was used. The i-speed 2 camera can make images at a maximum frame rate of 33,000 Hz and has a maximum frame rate at full resolution of 1,000 Hz. The resolution at 1,000 Hz and lower is 800 x 600 pixels, above 1,000 Hz the resolution decreases, down to a resolution of 96 x 72 pixels.The i-speed 2 camera is equipped with a CMOS sensor and can be controlled with computer software which is available for the camera. The CMOS sensor consists of 800 x 600 pixels and is 11.2 x 8.4 mm^2. A picture of the i-speed 2 camera is shown in figure 3.3.
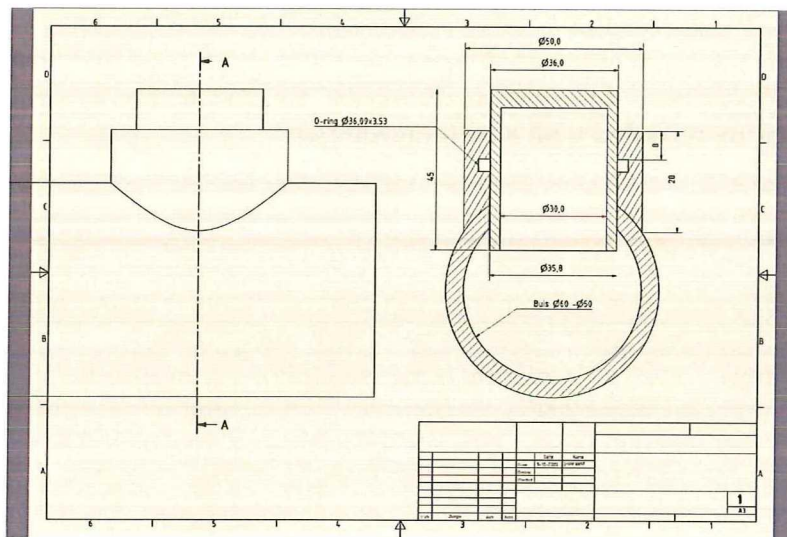
Figure 3.2: Schematics of the hole in the pipe. On the left, a view from the side of the pipe is shown, on the right the cross section of the pipe is shown.

Figure 3.3: Picture of the i-Speed 2 camera.

3.2.2   Lenses and spacers

For the camera several lenses are available with focal lengths of 8, 25, 50 and 75 mm. These lenses are placed in front of the CMOS sensor. With spacers of 1, 2, 5, 10, 20 and 40 mm, the distance from the lens to the CMOS sensor can be adjusted with a minimum distance of 14 mm. Enlarging the space between the lens and the CMOS sensor causes a smaller picture to be fitted on the CMOS. This means that the size per pixel on the CMOS sensor decreases. When the distance between the CMOS and the lens is increased, also the distance between the lens and the object at which a picture is sharp is decreased. For the 25 mm lens this is tabulated in table 3.1, for the 50 mm lens this is tabulated in table

3.2 and for the 75 mm lens this is tabulated in table 3.3. The 8 mm lens was also tested, but no useful results were obtained. Decreasing the size per pixel and keeping the same amount of pixels, the size of the picture decreases. This means that by using the spacers, smaller pictures are recorded with a better resolution.

Table 3.1: Resolution of a 25 mm lens with different distances to the CMOS sensor.

Space between lens and CMOS (mm)	Distance at which the picture is focused (cm)	Spatial resolution (μm/pixel)
18	9	56
23	6	31
28	3	21
33	3	16
41	2	13
106	-	-

Table 3.2: Resolution of a 50 mm lens with different distances to the CMOS sensor.

| Space between lens and CMOS (mm)	Distance at which the picture is focused (cm)	Spatial resolution (μm/pixel)
18	45	113
23	31	65
28	21	44
33	17	33
43	15	27
48	12	19
58	10	15

Table 3.3: Resolution of a 75 mm lens with different distances to the CMOS sensor.

Space between lens and CMOS (mm)	Distance at which the picture is focused (cm)	Spatial resolution (μm/pixel)
18	∞	-
28	28	45
38	21	31
48	18	24
58	15	21
78	15	16
106	12	11

3.2.3   Depth of focal field

Increasing the spacer length gives a decrease of the depth of the focal plane. In figure 3.4 a set-up for the measurement of the depth of focal plane is shown. Here the depth of the focal plane is about 4 mm. The depth of focal field can become very small, and therefore pictures can become fuzzy when movement is present. The optimal depth of focal field in combination with the best resolution is dependant on the circumstances in a specific case.

For the 50 mm lens the depth of field (DOF) was measured for different spacers, the results are given in table 3.4.
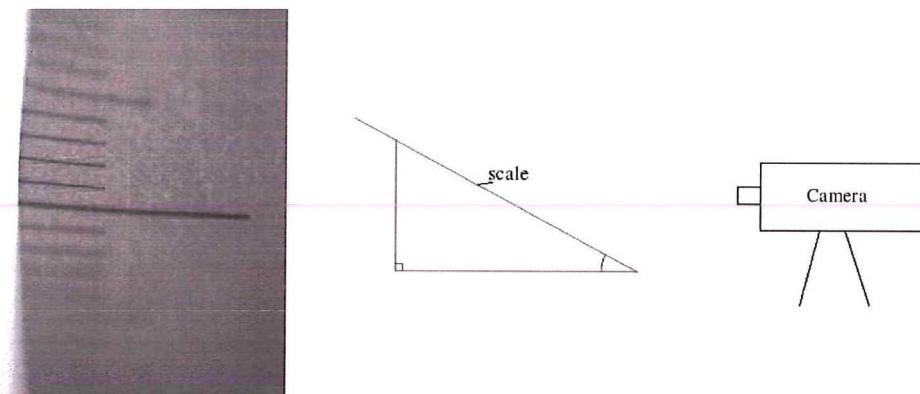
Figure 3.4: On the left a picture is shown with which the depth of the focal plane can be measured. The distance between the lines is 1 mm, so the depth of field is about 4 mm. The brightness and contrast of the picture have been changed for a better visibility. A lense of 75 mm is used with a distance of 44 mm between the CMOS and the lens. On the right the schematics of the experimental setup are shown. The angle of the scale with the horizontal is 27 degrees. From the picture on the left, it is seen that the depth of focal plane is about 4 mm.

Table 3.4: DOF of a 50 mm lens with different distances to the CMOS sensor.

Space between lens and CMOS (mm)	DOF (cm)
18	3.5
23	1.5
28	1.0
33	0.5
43	0.4
48	0.3
58	0.2

3.2.4   Conclusions

Comparing the requirements given in section 1.6 and the verifications given in this chapter, it is obvious that compromises on the best configuration have to be made. Since the

roll waves in annular flow are dynamic and three dimensional, the depth of field should at least be half a centimetre. From table 3.4 it is seen that this requires a 50 mm lens at 33 mm from the CMOS sensor. Using this lens at this distance from the CMOS sensor gives a spatial resolution of 33 μm/pixel and an image with an area of 2.6 x 2.0 cm^2. With this, droplets of around 150 μm in diameter can be visualised in an area of approximately half the tube diameter. From Marmottant et al. [23] it is known that ligaments can reach sizes up to 10 mm. Visualisation of these ligaments should be possible with the area given above.

In chapter 4 another lens configuration was used, the spatial resolution in this study was 56 μm/pixel. This was a preliminary study and from that study it was concluded that a better spatial resolution was needed to visualise the annular flow. The annular flow is visualised with the configuration given above. The camera was placed such that the area of the hole in the pipe was captured, this gives a slightly larger spatial resolution of 39.4 μm/pixel.
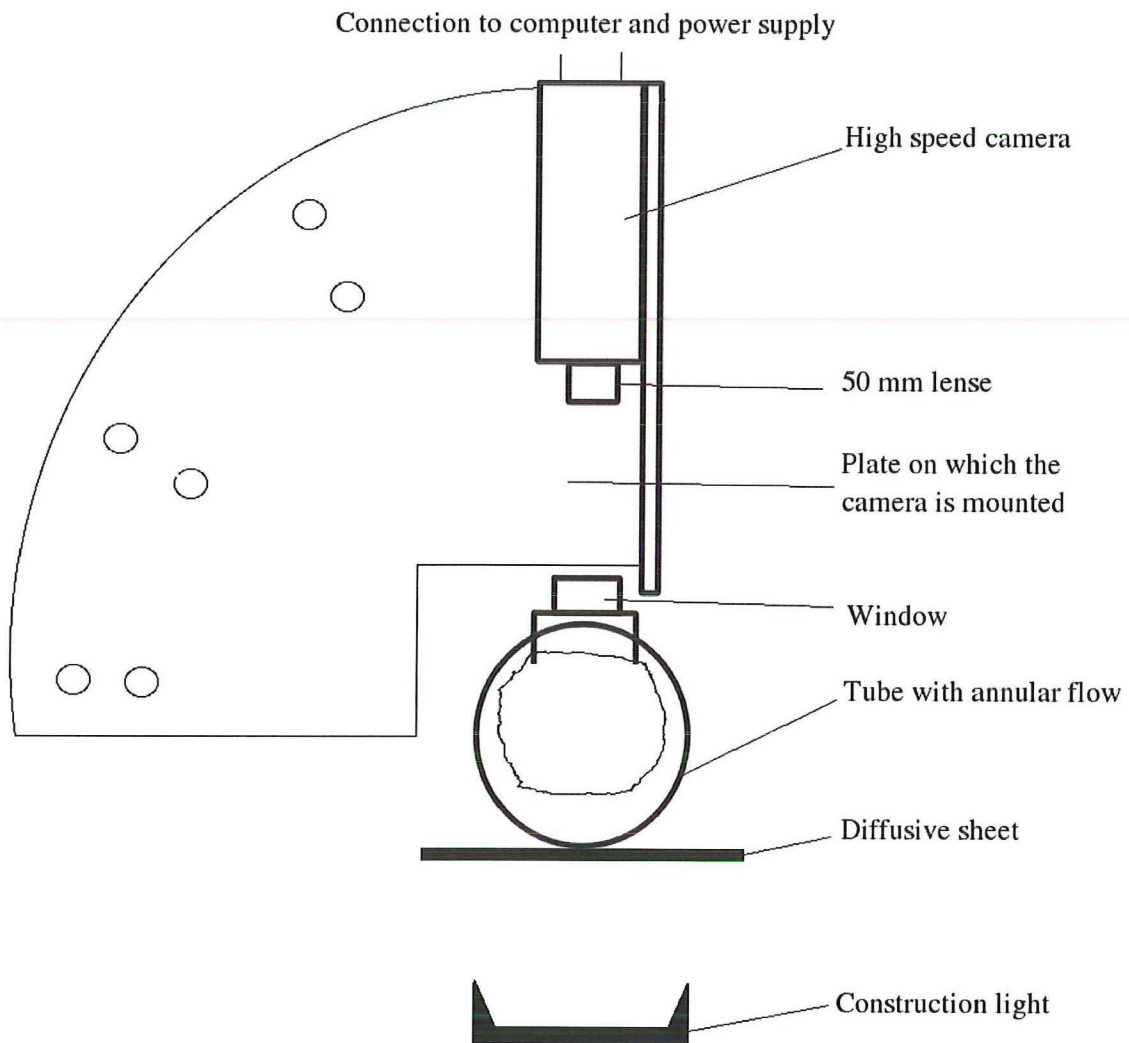
3.2.5   Possible improvements

From the conclusions given above it is clear that there is room for improvement in the use of the camera. One possibility is the use of a camera with a larger CMOS sensor, with this the spatial resolution can remain the same, while the size of the image is enlarged. A new camera is very expensive, so for this project this improvement was not made. Another option is to use a lens with a focal distance between 8 and 25 mm, with this the spatial resolution can be improved, with a larger depth of field. If such a lens is used, it should be kept in mind that the distance between the lens and the image plane is at least 6 cm. In this work no new lens was purchased since the the improvement was not expected to be significant and the costs for a new lens were high.

A last possibility is to use a high resolution camera with flash lights, as described by Marmottant et al. [23]. The disadvantage is that this setup cannot follow the entire evolution of the motion.

3.3   Experimental setup

To finalise the experimental setup, the camera, construction light and the flow pipe were combined as seen in figure 3.5. The construction light is needed to make sure enough light reaches the CMOS sensor. The camera is mounted on a plate, with holes in it, such that the camera can be positioned at angles of 0, 30, 60 and 90 degrees with respect to the pipe. The pipe can also be rotated, such that the window is faced to the camera. The construction light is always positioned in line with the camera and the window, behind the flow pipe. Between the pipe and the construction light, a sheet is placed in order to diffuse the light. The light, camera and the window should be placed exactly in line to construct the best pictures. The setup can be positioned at different distances downstream the water inlet.

Connection to computer and power supply

High speed camera

50 mm lense

Plate on which the
camera is mounted

Window

Tube with annular flow

Diffusive sheet

Construction light

Figure 3.5: Experimental setup used during the project. The setup is mounted on the frame of the
flow pipe, so it stays in place when the pipe is inclined. The camera is connected to a computer
with processing software.

Chapter 4

Stratified flow in a horizontal tube

4.1 Introduction

In stratified flow, the gas and liquid move in separated layers through the pipe, with superficial velocities of u_{sg} = 0 to 15 m/s and u_{sl} = 0 to 0.1 m/s. At low gas velocities, the liquid is at the bottom of the pipe and flowing smoothly. When the gas velocity is increased, the shear stress from the gas to the liquid grows and a more wavy pattern occurs. From this wavy pattern, droplets can be sheared off the wave crests and get entrained into the gas phase.

In this chapter on stratified flows some characteristics of the stratified flow are examined. The goal is to gain experience with the use of a high speed camera in investigating flow patterns. Data is presented on the onset of entrainment in stratified flow and the characteristics of ligaments in stratified flow. No attempt has been made to statistically verify the results, since the goal of this chapter is only to investigate the possibilities of working with the high speed camera.

For this preliminary investigation, the visualisation setup was placed at 2.7 m from the air inlet to collect images of the flow. Images were taken from a top view and from a side view to link entrainment mechanisms and entrainment rates. A lens with a focal length of 25 mm was used at a distance of 18 mm from the CMOS sensor, this gives a spatial resolution of 56 μm/pixel and an image of 4.5 x 3.6 cm^2. The frame rate was 1,000 fps. Examples of a stratified flow from top view and side view are shown in figure 4.1 and 4.2.
In figure 4.1, a side view of the stratified flow is shown. In the bottom the liquid layer is present and the focus is in the centre of the pipe. The liquid closer to the camera is out of focus, so the top of the liquid layer looks blurred while the bottom of the liquid l;ayer looks sharp. At the bottom of the layer some refractive patterns are visible. In figure 4.2 a top view of the stratified flow is seen with the focus at the gas/liquid interface.

4.2 Onset of entrainment

In stratified flow, different regimes are recognised. When flow rates of liquid and gas are changed, the flow can change from stratified smooth to stratified wavy and when the flow rates are increased annular flow appears. In flows that are stratified wavy, there is a point at which droplets get entrained in the gas. Azzopardi [5] and Hewitt et al. [15]
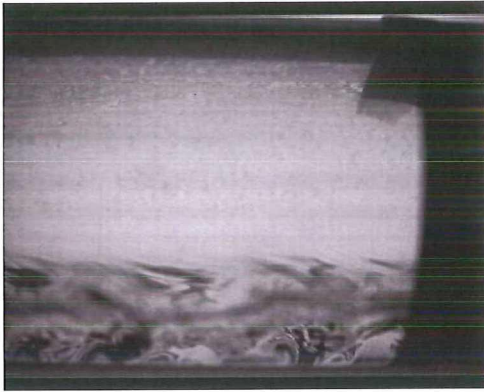
Figure 4.1: Stratified flow in a pipe, as viewed from the side. At the bottom of the pipe, water is present and at the top of the pipe air is present. The flow is from left to right and the size of the picture is 4.5 x 3.6 cm^2.

Figure 4.2: Stratified flow in a pipe, as viewed from the top. Here the same liquid and gas flow rates are used and the flow is from left to right and the size of the picture is 4.5 x 3.6 cm^2.

suggest that there are critical gas and liquid flow rates at which the onset of entrainment occurs.

In the present investigation, an attempt was made to make a chart in which the onset of entrainment is visualised. This chart is shown in figure 4.3. In figure 4.4 a comparison chart from Hewitt et al. [15] is given.

From the chart of Hewitt et al. it is shown that a critical liquid flow rate exists below which there is no entrainment. From the chart this critical liquid flow rate can be determined to be 1.3×10^{-4} kg/s with a liquid Reynolds number around 200. The present investigation does not consider low liquid Reynolds numbers so the limiting liquid flow rate cannot be confirmed. The limiting gas flow rate to which the results from Hewitt et al. [15] tend to go are not found here either, but roughly the same shape can be detected. From the comparative charts in figure 4.3 and 4.4 it can be seen that a whole different regime of liquid Reynolds numbers is found when looking for the onset of entrainment, while the regime of gas Reynolds numbers is about the same. An explanation for the different regime of liquid Reynolds numbers, might be the difference in pipe diameters. In the investigation of Hewitt et al. [15] a 1 cm pipe diameter is used while in the present investigation a pipe with 5 cm diameter is used.

## 4.3 Ligaments

4.3.1 Formation

When the gas velocity in stratified flow is increased, the liquid film gets more wavy and the possibility starts to exist that droplets are sheared off from the liquid film. Most of the droplets that shear off from the liquid film do so from ligaments. Ligaments are chunks of liquid that spat up in the stratified flow. An example of a ligament in stratified flow is shown in figure 4.5.

From movies taken with the high speed camera, it is seen that ligaments are formed almost instantaneously. When a wave passes, there is a chance that a ligament will tear off. The ligament gets entrained and within 0.002 seconds the ligament breaks into droplets.
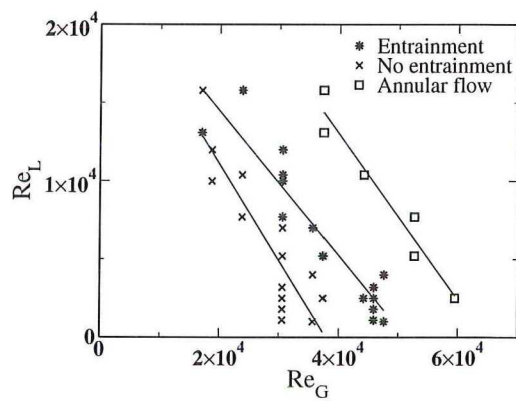
Figure 4.3: Onset of entrainment chart. In the lower left corner, no entrainment occurs. In the upper right, annular flow is present. In between stratified flow with entrainment occurs. The minimum liquid Reynolds number is around 800, so this plot roughly complements the plot in figure 4.4.
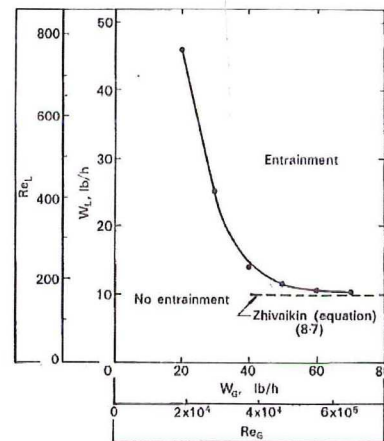
Figure 4.4: Typical plot marking conditions for the onset of entrainment, 10 lb/h means 1.3×10^{-4} kg/s. The data results from air-water flow in a 3/8 inch bore tube, Hewitt et al. [15]

Since the camera is focused on a small part of the pipe, only a fraction of the breaking ligaments is recorded. The formation of the ligaments takes a long path in which a wave crest is formed, until it breaks. This path of roll-wave formation is not recorded, so the process before ligament break up is not entirely understood.

4.3.2 Droplet velocity

In the event of ligament formation, the liquid in the ligament accelerates to a velocity which is larger than the velocity in the liquid layer. To see where this acceleration occurs, movies of ligament formation are analysed.

First, the ligament in figure 4.5 was examined. The velocities of the front and the back of the ligaments were measured by taking the number of pixels they move per frame. The velocity can then be calculated with $v = \frac{\Delta px \cdot R}{\Delta t}$, where Δpx is the number of pixels travelled, R is the spatial resolution and Δt is the time difference.

It was seen that the front of the ligament moves with an approximately constant velocity of 4.4 m/s in the direction of the flow. The back of the ligament also seems to travel with a constant velocity of 3 m/s. From this, it is concluded that the acceleration of the ligament occurs at the point where the ligament is formed, after this the ligament is torn apart due to the difference in velocity.

The average velocities of the gas and liquid can be estimated from the flow rates of the gas and the liquid. For the gas this becomes:

$$u_g = \frac{\dot{m}_g}{A_{gas} \cdot \rho_g} \tag{4.1}$$

And for the liquid this becomes:

$$u_l = \frac{\dot{m}_l}{A_{liq} \cdot \rho_l} \tag{4.2}$$
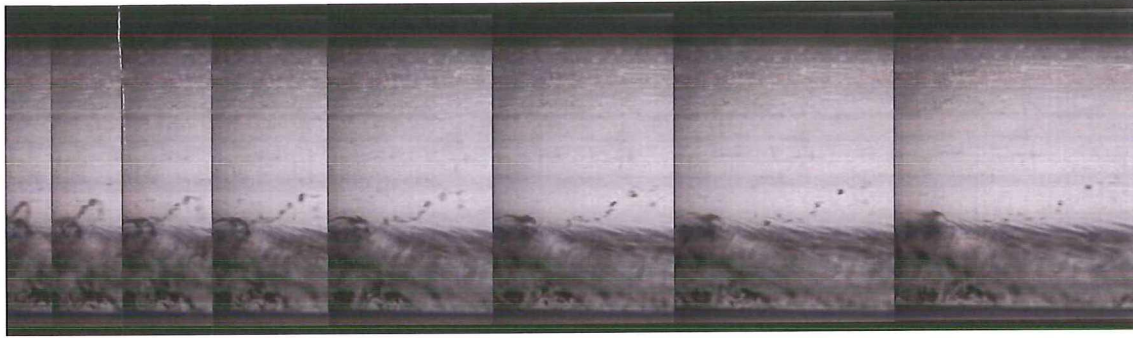
Figure 4.5: Ligament break up at a superficial liquid velocity of 0.03 m/s and a superficial gas velocity of 12 m/s. The time between each frame is 0.001 s.

The perpendicular area is the area of the pipe in which the gas or the liquid flows. The liquid covers about 25 % of the area and the gas approximately 75 %. The total area is 19.6 cm^2. Considering values for the mass flow rate of the liquid of 0.052 kg/s and for the volumetric flow rate of gas of 0.023 m^3/s, the average gas and liquid velocities are: u_g= 15 m/s and u_l= 0.1 m/s. The values of the gas and liquid velocity are average values, the actual value of the liquid at the gas/liquid interface has an intermediate value. The superficial gas and liquid velocities are defined as:

$$u_{sg} = \frac{A_{gas}}{A_{pipe}} u_g \qquad\qquad u_{sl} = \frac{A_{liquid}}{A_{pipe}} u_l \qquad\qquad (4.3)$$

Where $A_{subscript}$ is the frontal area of the phase in the pipe. For the droplets, the drag force in the direction of the flow, can be compared to the gravitational force. The drag force is given by:

$$F_d = C_d \frac{1}{2} \rho (u_g - u_{drop})^2 A_\perp \qquad\qquad (4.4)$$

And the gravitational force is given by:

$$F_g = \frac{4}{3} \pi r^3 \rho g \qquad\qquad (4.5)$$

Using the values found in the experiment, the drag force is found to be in the order of 0.1 N and the gravitational force is in the order of 10^{-5} N. This means that the drag force is 4 orders of magnitude larger, so the vertical velocity of the droplets is negligible compared to the horizontal velocity.

4.3.3 Angle

In recovering ligaments from movies, made with the i-speed camera, a wide range is found in the angles at which ligaments are torn from the liquid film. This angle is shown schematically in figure 4.6. Data on the angles can only be collected from side view movies. The disadvantage of the side view movies is that there is a small region in which the movie is focused, this causes ligaments to be blurry or sometimes even hardly visible. Some ligaments could be recovered from the movies and two examples of these are shown in figures 4.7 an 4.8.
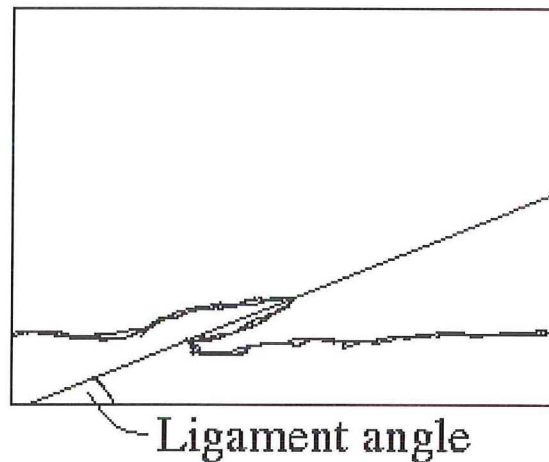
Ligament angle

Figure 4.6: Definition of the ligament angle, the lower layer in this graph is the liquid layer and the upper layer is the gas layer. A ligament is torn from the liquid layer and the definition of the angle is given in the graph.

Table 4.1: Angles with which ligaments are torn from the liquid surface at different superficial velocities. The data show that it is possible to measure ligament angles in several flow conditions.
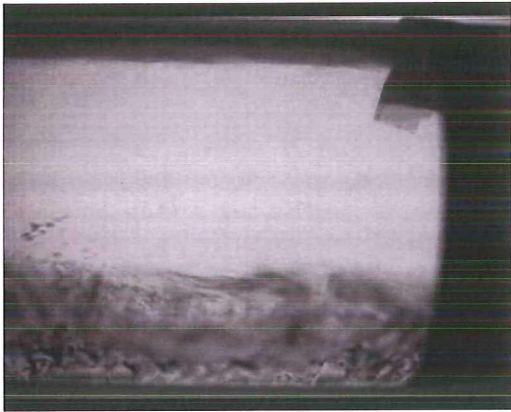
Superficial liquid velocity (m/s)	Superficial gas velocity (m/s)	Angle (°)
0.026	7.0	44
0.026	7.0	41
0.040	9.5	49
0.055	11.5	29
0.065	13.5	9
0.080	15.5	58

From the recorded ligaments, the angle with which they are released into the gas core is measured. It follows that there is a wide range of release angles at different flow rates. The data on these angles is summarised in table 4.1. Note that this is just a small example to illustrate the possibilities of the measurements of ligaments and no attempt was made to make a statistical validation of the measurments of the ligament angles.

4.3.4 Size

The size of ligaments entraining in the gas core is of interest. In order to measure this, the pictures from the top view and the side view are linked. Since there is only one camera available, the pictures of the ligaments are not of the same ligament, but the pictures are made using the same flow rates for the gas and the liquid. Pictures of a ligament are given in figures 4.9 and 4.10.
From the pictures of the ligaments, the ligament area can be determined since the size of the pixels is known. For the pictures in figure 4.9 and 4.10, the area is determined to be of the order of 5 mm^2. Assuming the ligament to be cylindrical shaped, the volume of the

Figure 4.7: Ligament torn from the liquid film with a superficial liquid velocity of 0.06 m/s and a superficial gas velocity of 13.5 m/s. The flow is from left to right.
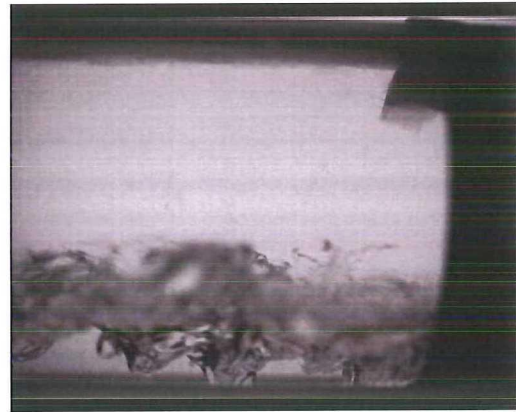
Figure 4.8: Ligament torn from the liquid film with a superficial liquid velocity of 0.07 m/s and a superficial gas velocity of 11.5 m/s. The flow is from left to right.
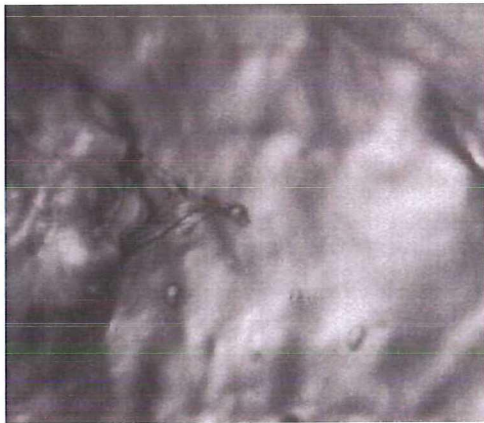
Figure 4.9: Top view of a ligament with a superficial liquid velocity of 0.055 m/s and a superficial gas velocity of 13.5 m/s. The flow is from left to right.

Figure 4.10: Side view of a ligament with a superficial liquid velocity of 0.055 m/s and a superficial gas velocity of 13.5 m/s. The flow is from left to right.

ligament is determined to be around 10 mm^3.

When a ligament evolves, it breaks up in multiple droplets and the size of the droplets can be determined from the pictures. In figure 4.10 the droplets already start to form. The droplet sizes in the ligament range from 0.15 to 1.2 mm^2 (or 0.2 to 0.6 mm in equivalent diameter) and the total area occupied by the droplets is 4 mm^2, these sizes were captured from a picture taken 0.003 seconds after the picture in figure 4.10.

In this investigation, pictures were analysed on sight. When pictures like this need to be processed in an automated way, software like DIPimage or NIH image software will be necessary.

4.4 Conclusions

From this preliminary study on stratified flow in a horizontal pipe, some concluding remarks can be given. First of all, it is possible to produce an onset of entrainment plot and with enough measurement data this can be compared to existing data on this topic. For the flow loop used here, this would be an improvement on the existing data. This onset of entrainment chart is no part of the focus of this investigation, so will not be worked out here. This might be a topic for future investigation on stratified flow.

From the part on the ligaments in stratified flow it is seen that there are a lot of mechanisms involved in the dynamics of ligaments. The formation of ligaments is a larger process than captured in the view of the camera. The instantaneous formation of a ligament on top of a roll wave is captured, so conclusions can be drawn from that. For more insight in the formation of ligaments a better understanding of the formation and break up of roll waves is necessary and more investigations on this topic needs to be done.

When droplets are entrained in the gas core, they are already at their final velocity. The difference in velocity at the top and the bottom of the ligament causes it to break into droplets. From this it is seen that the acceleration of the droplets occurs when the ligament is still in the roll wave. When the droplets are entrained, their velocity is mainly in the direction of the air flow. This is explained by a large difference between the drag force and the gravitational force, working on a droplet.

When the angles of the ligaments are considered, a wide spread in the angles at which ligaments are torn of the liquid film is observed. However, the majority of the angles lie around 40 degrees. For good statistics on the angles with which the ligaments are torn of the liquid film, lots of pictures of ligaments are needed. The same holds for the determination of the sizes of the droplets from the ligaments. For good statistical results, image processing software is needed. As mentioned in the introduction of this chapter, no attempt has been made to statistically verify the data gained. The goal was to gain experience on working with the high speed camera and explore its possibilities.

Chapter 5

Annular flow in a horizontal tube

5.1 Topology of the liquid film

In annular flow, different structures of the liquid surface appear. There is a part in which a rippled surface exists, followed by a part called roll wave or disturbance wave. In between the ripples and the roll waves a transition region is present. This is described by Hall-Taylor et al. [11]. A picture of these structures, made by Hall-Taylor can be found in figure 5.1.

Belt [6] states the existence of ephemeral waves, which look similar to roll waves but they are much less coherent. The ephemeral waves are smaller than roll waves and occur less frequent. Also their velocity differs from the roll-wave velocity, causing them to merge with a roll wave. Therefore, ephemeral waves have a short life time. In the current setup, it is not easy to distinguish the difference between roll waves and ephemeral waves. Ohba et al. [25] also mention waves which are different from disturbance waves, their velocity is lower than the disturbance wave velocity, which reduces their time of existence. Ohba et al. call these waves 'ring waves'.

The topology of the liquid film in annular flow is investigated at a distance of 8.5 meters (170 pipe diameters) from the water inlet. In the investigation, several combinations of superficial gas and liquid velocity are encountered. For the different gas/liquid velocity combinations, the ripple-wave part and the roll-wave part will be thoroughly investigated. Results on the ripple-wave regime will be reported in chapter 6. In chapter 7 and 8 the details of the roll waves are considered. In chapter 7 results on phenomena like the roll-wave frequency and velocity will be reported and in chapter 8 the structure of the roll waves is explained in detail.

5.2 Development length

An important aspect in the investigation of annular flow is the development length Z_{eq}, which is the distance required to reach hydrodynamic equilibrium between the entrainment and deposition of droplets onto the liquid film. A correlation for the development length is given by de Bertodano et al. [8]:

$$\frac{Z_{eq}}{D} \approx 440 \frac{We^{0.25}}{Re_L^{0.5}} \tag{5.1}$$
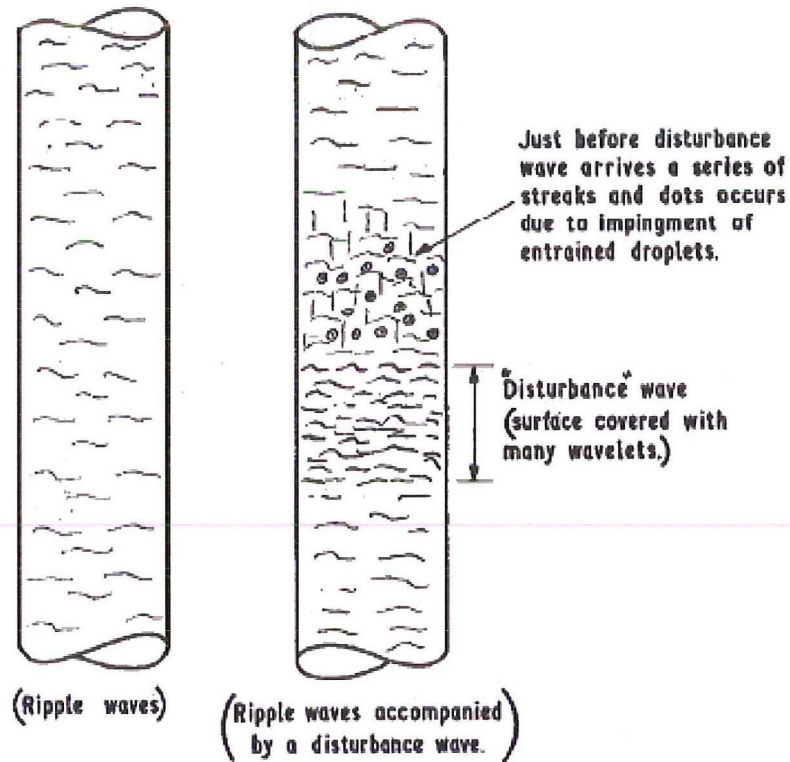
Figure 5.1: Schematic view of the different patterns of the liquid surface in 2-phase annular pipe flows, Hall-Taylor et al. [11].

Where the Weber number is defined as:

$$We = \frac{\rho_g u_{sg} D}{\sigma} \left(\frac{\Delta \rho}{\rho_g} \right)^{1/3} \tag{5.2}$$

And the liquid film Reynolds number is defined as:

$$Re_L = \frac{\rho_l u_{sl} D}{\varepsilon_l} \tag{5.3}$$

Here, D is the tube diameter, ρ_g and ρ_l are the gas and liquid densities, $\Delta \rho$ is the density difference, σ is the surface tension and ε_l is the dynamic viscosity of the liquid.
For a superficial gas velocity of 34 m/s and a superficial liquid velocity of 1.2 cm/s, $\frac{Z_{eq}}{D}$ becomes 171. With a pipe diameter of 5 cm, this means a distance of about 8.5 meters. This is the u_{sl}, u_{sg} combination encountered with the highest development length. The current measurements where performed at a distance of 8.5 meters from the water inlet, so hydrodynamic equilibrium can be assumed.

Chapter 6

Ripple waves in horizontal annular flow

The structure of ripple waves in annular flow was investigated by, amongst others, Asali et al. [3] and by Belt [6]. Asali et al. [3] measured the ripple spacing from photographs taken through a transparent flow pipe. The film thickness of the liquid film was measured by both Asali [3] and Belt [6] by use of a conductance probe. With this probe it is possible to determine the mean film thickness and to measure the roll waves, but determination of the ripple height is still difficult, since the conductance probe lacks the resolution. Asali [2], [3] states that the ripple height is 10 to 20 μm with wavelengths of 2 to 3 mm at low liquid flow rates.

In this chapter, the possibilities of measurements on the ripple waves are described to see to what extend it was possible to reproduce the results from Asali.

6.1   Ripple-wave analysis

In order to analyse the ripple waves in horizontal annular flow, pictures of rippled surfaces were made at different gas flow rates. Examples of these pictures are shown in figures 6.1 and 6.2. The pictures show ripple waves at two different flow rates and the size of the pictures is the same. What is observed in the pictures is that the liquid surface with a higher gas flow has more ripples, but these ripples are smaller in size. On average the ripples have a vertical inclination in the pictures, i.e. perpendicular to the flow.

Using image analysis software, it is possible to collect data out of pictures like this, which will contain the orientation and the size of the ripples; with this information, the topology of the rippled surface can be modelled. The possibilities for automating the ripple-wave analysis with a wavelet transform approach were investigated, but so far this investigation has not proven itself. The theory behind the wavelet approach will be discussed at the end of this chapter.

Since the wavelet transform approach did not work out for now, the ripple waves were investigated by visual inspection. Results are given on the ripple-wave dimensions, the orientation of the ripples and the velocity. The visual inspection is a time consuming task, so only a small sample size was investigated. For further investigation, automation of the ripple-wave analysis is needed.
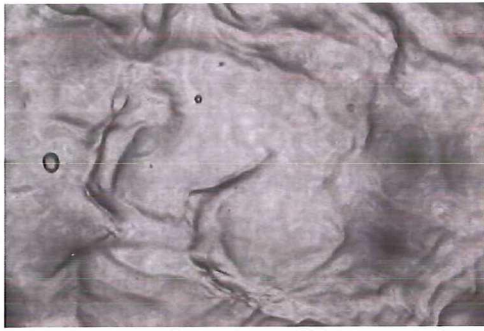
Figure 6.1: Rippled surface for flow in a horizontal pipe, at a superficial liquid velocity of 1.2 cm/s and a superficial gas velocity of 22 m/s. The width of the picture is 2.4 cm and the height is 1.6 cm. The flow is from right to left.


Figure 6.2: Rippled surface for flow in a horizontal pipe, at a superficial liquid velocity of 1.2 cm/s and a superficial gas velocity of 28 m/s. The width of the picture is 2.4 cm and the height is 1.6 cm. The flow is from right to left.

6.2 Quantities in ripple-wave analysis

6.2.1 Spatial resolution

In order to analyse different dimensions of the ripple waves from the pictures, the spatial resolution with which these quantities can be measured needs to be determined. To determine the spatial resolution, a ruler is placed at the position of the ripple waves, a picture of this is shown in fig 6.3.

From the picture of the ruler, the spatial resolution of the camera can be determined. The number of pixels between 14 millimetres of distance is 356, so this gives a spatial resolution of 39.4 μm per pixel. The lines of the ruler are not very thin, about 6 pixels, so there is an error in the 14 millimetres of $\pm$ 6 pixels or $\pm$ 0.24 mm. This gives an uncertainty in the spatial resolution of 0.6 μm, so the spatial resolution at this point is 39.4 μm $\pm$ 0.6 μm, per pixel this attributes to an uncertainty of 1.5 %.
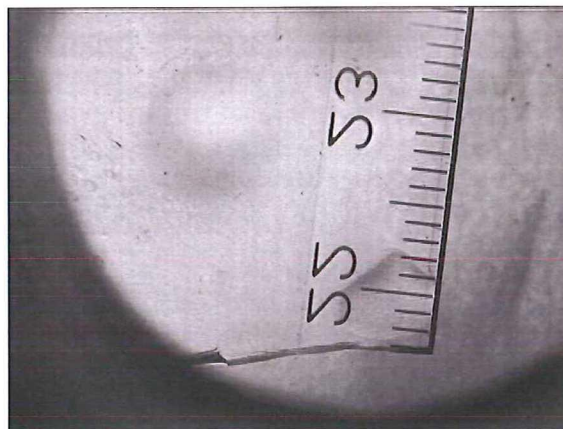
Figure 6.3: Ruler placed at the same position as the liquid film in the tube.

6.2.2   Definition of ripple-wave dimensions

Now that the resolution with which the ripples can be determined is known, a number of definitions of the ripple-wave dimensions is needed. The schematics of the different dimensions are given in figure 6.4. In figure 6.4 the length of the ripple is indicated, which is different from the conventional wave length, denoted by the spacing. Furthermore, information on the wave height, wave width and angular orientation of the ripple waves is required in order to give a good description of the ripple-wave topology.

The dimensions are determined from visual inspection, for the length, width and spacing the number of pixels for each quantity is determined. For the ripple-wave length, the relative error in determining the number of pixels is not bad. The edges at the ends of the ripples are quite clear. With a typical ripple-wave length of 3 mm, an error of two pixels would mean a relative error of 3 %.

For the width, the relative error is larger, since it is not very clear where the ripple edges are. The centre of a ripple is well defined as the part of the ripple which is the darkest. Moving away from the centre, the ripple must end somewhere, but the edge of the ripple and the start of the flat liquid surface is not well defined. From this, a large uncertainty follows. When a typical ripple-wave width of 0.3 mm is considered and an error of 3 pixels, the relative error grows to 40 %.

No attempt has been made on determining the ripple spacing. This quantity is hard to define since the ripples do not move as a well-aligned structure with only one orientation angle. In figure 6.1 it can be seen that the ripples move at several angles, the distance between each ripple is then ill-defined and open to a lot of arbitrariness.

Determination of the height of the ripple waves is not possible from the pictures made with the current set-up. A good possibility for ripple-wave height determination is by the use of stereo imaging. For this two cameras are needed, in order to make images with a certain overlap. A short introduction on this technique is given in appendix B.
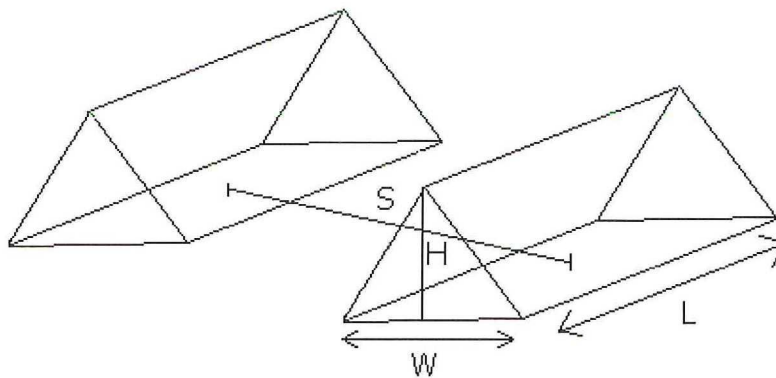

Figure 6.4: Schematics of ripple waves in annular flow, the ripple-wave length (L), width (W) and height (H) are indicated, together with the spacing (S) between the ripples. This is a schematic 3D impression of the ripples given in figures 6.1 and 6.2.

6.2.3   Ripple-wave orientation

The orientation of the ripples in the flow is an important parameter in the description of the surface topology of the liquid surface in annular flow. In figure 6.5 the definition

used for the orientation of the ripples is given.

The ripple-wave orientation was investigated by visual inspection. In order to do so, straight lines were drawn through the ripples and the angle was determined. In reality, the ripples are not straight lines, so the determination in this way is a bit arbitrary. From symmetry reasons and from a quick look at the pictures in figures 6.1 and 6.2 one would expect the average ripple-wave orientation to be around 0 degrees.
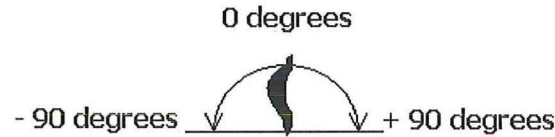
Figure 6.5: Schematics for the ripple-wave orientation, for ripples like given in figures 6.1 and 6.2. The black ripple is now situated at 0 degrees, but ripples are found between -90 and +90 degrees. The flow in this representation is from right to left.

6.2.4   Ripple-wave velocity

To analyse the velocity of ripple waves on the liquid surface, ripples on the surface are followed for a couple of frames. The distance travelled, combined with the time difference is a measure for the velocity.

Since not all the ripple waves have the same velocity, ten ripple waves per combination of superficial liquid and gas velocity are followed. The average ripple-wave velocity is determined as:

$$\bar{u}_{ripple} = \frac{1}{n} \sum_{i=1}^{n} u_{ripple,i} \tag{6.1}$$

For the statistical uncertainty the following equation is used:

$$u = \sqrt{\frac{1}{n(n-1)} \sum_{i=1}^{n} (u_{ripple,i} - \bar{u}_{ripple})^2} \tag{6.2}$$

Here, n is the number of ripple waves examined. The ripple waves only exist for a short period of time (4 ms or less), so the coherence between the sequential frames is low. For the determination of the position of a ripple, the centre of a ripple is followed. Since the coherence between the frames is low, this adds an uncertainty to the ripple-wave velocity of about 10 %.

6.3   Results from visual inspection

6.3.1   Ripple-wave dimensions

Length

The ripple -wave length for the ripple patterns in figures 6.1 and 6.2 was examined. The results are given in figures 6.6 and 6.7. From the figures it is seen that the ripple waves

for the lower liquid velocity are longer and that there are less ripples present in an area of the same size.

The average ripple length for a superficial gas velocity of 22 m/s is 2.5 mm while for a superficial gas velocity of 30 m/s the average ripple-wave length is 1.5 mm, the superficial liquid velocity is 1.2 cm/s for both cases.

The number of ripples is also different for both cases, the case with u_{sl}=1.2 cm/s and u_{sg}=22 m/s has 48 ripples, while the u_{sl}=1.2 cm/s and u_{sg}=30 m/s case has 69 ripples in an area of the same size. The numbers presented on the ripple-wave length confirm the idea given in section 6.1.
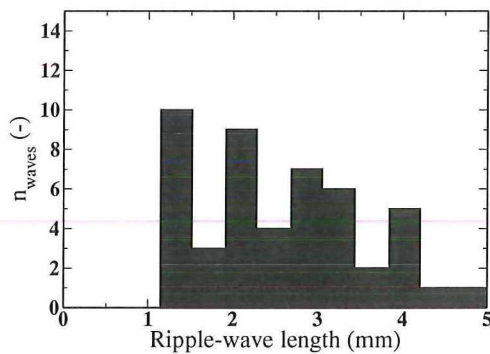
Figure 6.6: Distribution of the ripple-wave length for u_{sl}=1.2 cm/s and u_{sg}=22 m/s. The average ripple-wave length is 2.5 mm and a total of 48 ripples is examined.
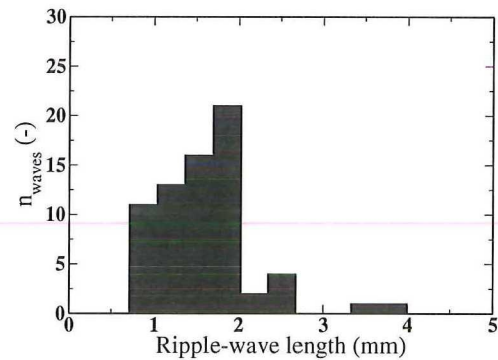
Figure 6.7: Distribution of the ripple-wave length for u_{sl}=1.2 cm/s and u_{sg}=30 m/s. The average ripple-wave length is 1.5 mm and a total of 69 ripples is examined.
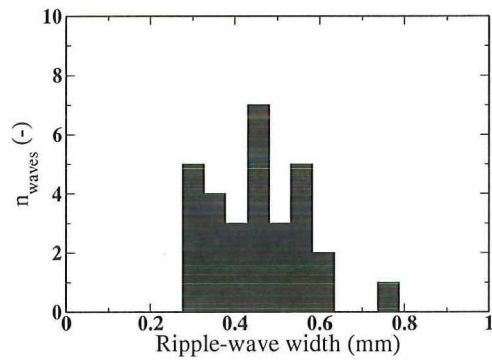
Width

For the width of the ripple waves, the ripples in the pictures of figures 6.1 and 6.2 were examined. For each picture, 30 ripple waves were selected and the distributions and mean ripple widths were determined. The ripple width for picture 6.1 is 0.5 mm, with a statistical uncertainty of 0.02 mm, the distribution of the ripple widths is given in figure 6.8. For the ripples in figure 6.2 also 30 ripple waves are selected and the mean ripple width is 0.3 mm with a statistical uncertainty of 0.02 mm, the distribution of the ripple widths is shown in figure 6.9.
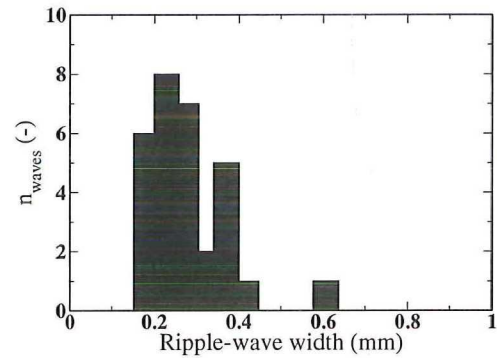
6.3.2   Ripple-wave orientation

From symmetry reasons, the flow should on average be symmetric, with the axis of the pipe as the axis of symmetry. This means that the ripple-wave pattern should also be symmetrical in this axis. To visualise this, the camera is carefully aligned above the centre of the pipe and the result is shown in figures 6.1 and 6.2. These pictures also suggest that the ripple-wave orientation is symmetrical.

From the figures, data on the orientation of the ripples is drawn by hand and the result is given in figures 6.10 and 6.11. There is a peak around the zero degrees orientation, which is expected from the symmetry argument. For the case with u_{sl}=1.2 cm/s and u_{sg}=22 m/s, there are peaks around -70 and +60 degrees. This symmetry does not occur for the distribution of the ripple waves in figure 6.10. This doesn't mean that on average there is
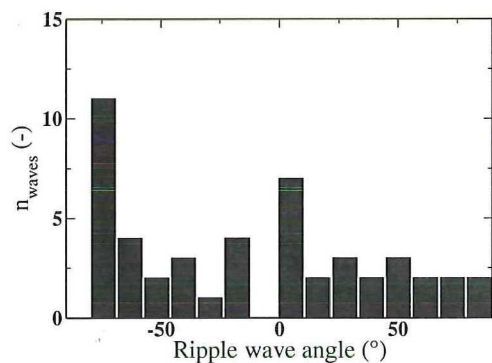
Figure 6.8: Ripple-wave width distribution for annular flow with u_{sl}=1.2 cm/s and u_{sg}=22 m/s. The mean ripple width is 0.5 mm.
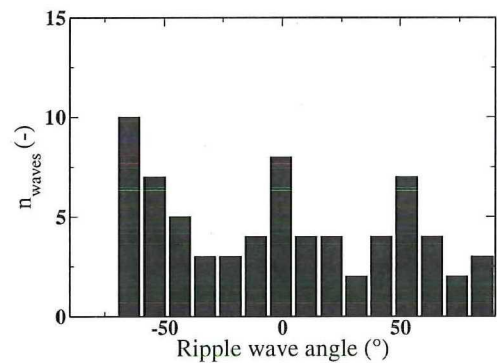

Figure 6.9: Ripple-wave width distribution for annular flow with u_{sl}=1.2 cm/s and u_{sg}=30 m/s. The mean ripple width is 0.3 mm.

no symmetry, but in this particular picture the symmetry is off.

Figure 6.10: Distribution of the ripple-wave orientations for the ripples in figure 6.1


Figure 6.11: Distribution of the ripple-wave orientations for the ripples in figure 6.2
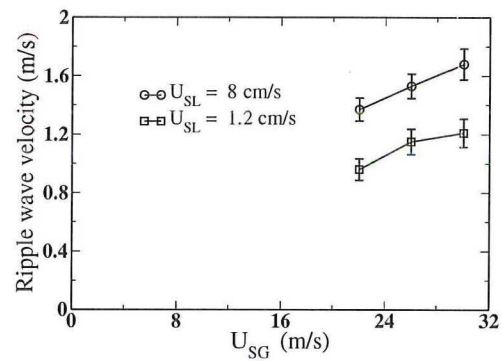
6.3.3   Ripple-wave velocity

In figures 6.12 and 6.13 the average ripple-wave velocities for several combinations of superficial liquid and gas velocities are shown. The error bars correspond to the statistical uncertainty from equation 6.2. What is seen is that the ripple-wave velocity grows with superficial gas and liquid velocity. However, when the superficial liquid velocity reaches a value of 8 cm/s, the ripple-wave velocity stagnates.

When the ripple-wave velocity is kept at 8 cm/s, the behaviour seems to be linear with superficial gas velocity. Since only 3 data points are considered here, firm conclusions on this behaviour can not be drawn.

It is hard to draw firm conclusions on the ripple-wave velocity. The ripples have a typical life time around 4 ms, so the coherence between the sequential frames is low.
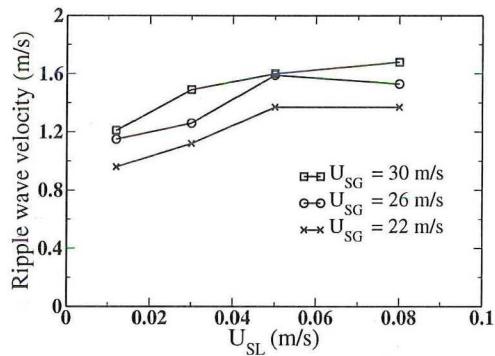
Figure 6.12: Ripple-wave velocities with their uncertainties for different combinations of superficial liquid and gas velocities.

Figure 6.13: Plot of the ripple-wave velocities versus superficial gas velocities. It seems that there is a linear relationship between the ripple velocity and the superficial gas velocity when the superficial liquid velocity is 8 cm/s. For the superficial liquid velocity of 1.2 cm/s this linear behaviour is not seen.
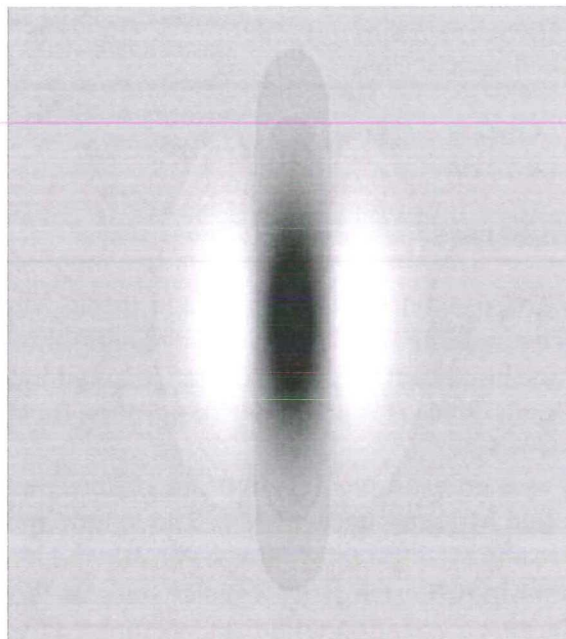
6.4   Wavelet transforms

In order to give a good representation of the average ripple-wave orientation, a lot of pictures in the ripple-wave regime must be analysed. Doing this by hand is a time consuming task and one must be careful to be consistent. To avoid inconsistencies, a wavelet approach is suggested, with which it is possible to determine the ripple-wave orientation and spacing in a consistent way.

The wavelet approach uses an example of a two dimensional wave which is shown in figure 6.14, it is a so called Mexican-hat wavelet. The length and width of the wavelet can be adjusted, but once adjusted the ratio between width and length is set. The wavelet program starts by comparing the size with wavelet sizes in the pictures of the ripple waves. The size with the best correlation with the structures in the pictures is chosen and then the angle of the wavelet is determined. The angles between 0 and 180 degrees are tested and the angle with the highest correlation is chosen. The program remembers the settings from a previous picture and stars for a new determination of the size at the angle that was the best angle in the previous picture.

When the correlation of the wavelet is set out against the ripple-wave orientation, pictures with a shape like in figures 6.10 and 6.11 are expected. When the pictures were examined, it was seen that this does not happen. The edges of the pictures have a large effect on the value of the correlation. At the top and the bottom of the picture, a large discontinuity is visible. This discontinuity is seen by the wavelet and the value of the correlation grows due to this.

We did not find a solution to the discontinuity at the upper and lower edge of the picture, so results from the wavelet are not shown. If the problem is solved, the wavelet transform approach coul to be a promising technique to verify the ripple-wave orientation and length.

Figure 6.14: Mexican-hat wavelet, as used in the wavelet transform program. The wavelet size and orientation is compared to the structures in the pictures of the ripple waves and the orientation and size with the highest correlation are used.

Chapter 7

Roll waves in horizontal annular flow

7.1   Roll-wave structures

In figure 7.1 a time series of a roll wave passing by is shown. The size of the view in the pictures is about 3.2×2.4 cm^2, this gives the same spatial resolution as in chapter 6: 39.4 μm/pixel. In the roll waves a lot of activity is going on. The roll wave is a part in the liquid film, where the film thickness is larger than the average film thickness. Just above the liquid film, ligaments occur from which droplets get entrained into the gas core. The velocities of the different droplets vary a lot. A couple of the droplets accelerate such that they get in front of the roll wave, there they impinge into the liquid film. Other droplets stay with the roll wave, at the same velocity, most of the time these droplets are larger than the accelerated droplets, around 1.0 to 1.5 mm in diameter. A schematic view of the roll wave is given in figure 7.2.

The view of the picture in figure 7.2 slightly deviates from the view by Hall-Taylor et al.[11], figure 5.1. They look at the roll wave as an actual wave with different wavelengths and heights. From figure 7.2 it is seen that the roll wave is actually a coherent moving disturbance with droplets and ligaments on top of a rippled liquid layer. The droplets in front of the roll wave, impinge in the liquid film as mentioned by Hall-Taylor et al.

7.2   Roll-wave macro-properties

In analysing roll waves, several macro-properties that characterise the roll wave as a whole are of importance. The focus here lies on the roll-wave velocity, frequency and length. The study of Paras et al. [26] also examine these quantities, using a parallel wire conductance technique combined with visual observations in a flow pipe with an inner diameter of 5.08 cm. Paras et al. only report data on large disturbance waves, so data on their roll-wave length is expected to be higher than data in this thesis and their roll-wave frequency is expected to be lower. This is because in the present study all the roll waves are considered, including the smaller ones. The ephemeral waves and ring waves, mentioned in section 5.1, were also seen as roll waves.

The measurements of the roll-wave quantities are performed at 8.5 meters from the water inlet, to ensure a well-developed flow, the measurements done by Paras et al.are performed at 15 meters from the inlet. Maybe some differences may occur, since the present measurements are performed at the development length (section 5.2), and the measurements from Paras well beyond that.
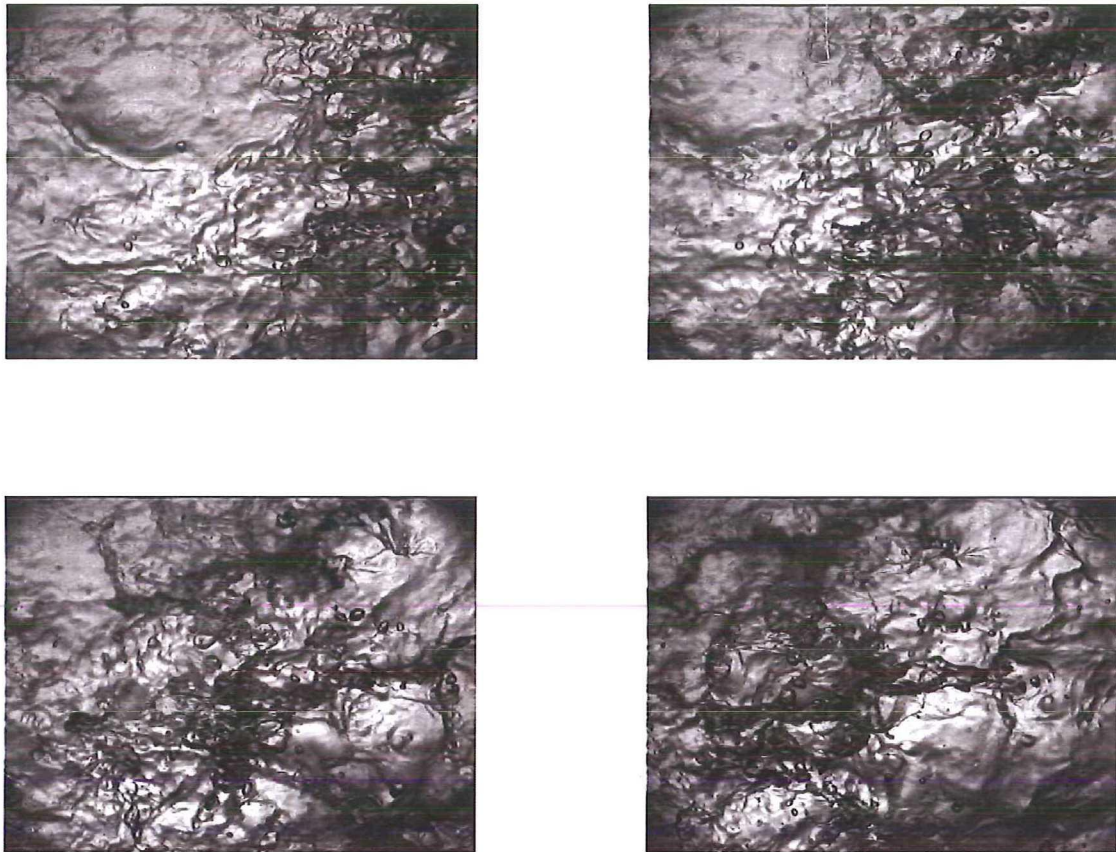
Figure 7.1: Picture of a roll wave passing by, the time between the frames is 2 ms. The roll wave enters the field of view at the picture in the top left, the picture at the top right shows the preceded contour of the roll wave. In the picture at the bottom left the roll wave occupies the whole field of view. At the bottom left the roll wave is leaving the field of view; the contour of the back of the roll wave is visible. The size of the pictures is 3.2 x 2.4 cm.

In this section, the different measurement techniques are explained and results from this are given in the next section. In the last section of this chapter, the results from the present study are compared to the results from Paras et al.[26].

7.2.1   Velocity

Measurement technique

Roll waves move with a certain velocity. From the movies, estimates can be made on the velocities of the roll waves. By visual inspection, the front of the roll wave is detected and followed through the frames. The time it takes for a roll wave to move from the right edge to the left edge of the field of view is determined. The width of the picture, 3.2 cm, is divided by this time and from this an average velocity of the front of the roll wave is determined. The assumption is made that the roll wave moves with a constant velocity. The accuracy of the position of the front of the roll wave is a bit arbitrary, since the shape of the roll wave is quite chaotic. Due to the chaotic shape of the front of the roll wave, it is possible that there is an uncertainty in the determination of the number of frames. For
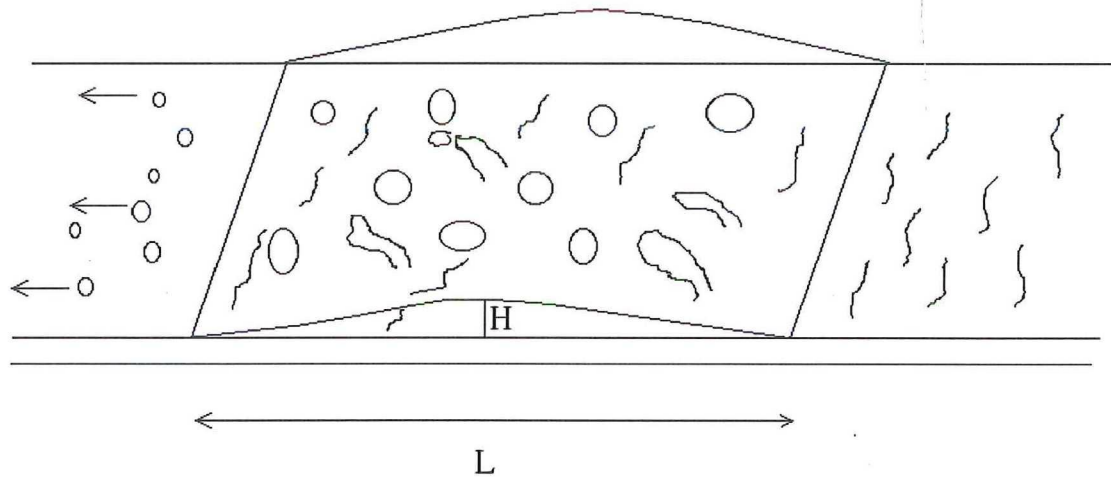
Figure 7.2: Schematic view of a roll wave in the tube, as observed from the pictures of the high speed camera. L is the length of the roll wave which is typically 1 to 5 cm and H is the film thickness which is typically 100 μm to 1 mm. The flow is from right to left and in front of the roll wave small droplets with a high velocity are present. These droplets impinge into the liquid film in front of the roll wave. The roll wave itself exists of droplets and ligaments on top of a liquid layer with ripple waves.

a typical roll wave, this gives an uncertainty of 2 frames. With a velocity of 1.5 to 4 m/s, this results in an uncertainty up to 20 %.

Automation of the measurements

In order to automate the velocity determination of the roll waves, a Matlab routine was written. In this Matlab routine, the time at which a roll wave passes is recorded and an attempt is made to follow the front of the roll wave. In order to follow the front of the roll wave, a contour plot of the roll wave was made and the average and front position of the roll-wave contour were determined. An example of a roll wave with its contour plots is shown in figure 7.3.

The positions of the front and the average position of the contour were recorded and plotted against time. An example of the positions of the average and front positions of the contour in time is given in figures 7.4 and 7.5. The position is given on the y-axis, the value is the pixel position. When the pixel value is high on the left, the roll wave enters the field of view and when the pixel value is low in the centre the roll wave leaves the field of view. The interpretation of the figure is not straight forward: To be able to find the roll-wave velocity from the figures, the data needs to be manipulated.

In order to find the point of entry and exit of the roll wave to the field of view, a 4th order polynomial fit was imposed. For the velocity determination, the time difference between the local maximum on the left of the plot and the local minimum in the centre of the plot is taken. With this time difference and the known distance, the average roll-wave velocity is calculated with $\bar{u} = \frac{\Delta x}{\Delta t}$.

The 4th order polynomial can have different shapes, and the program is build to find the correct position of the 2 points of time. The Matlab routine with which the roll-wave velocity is determined is given in appendix C.
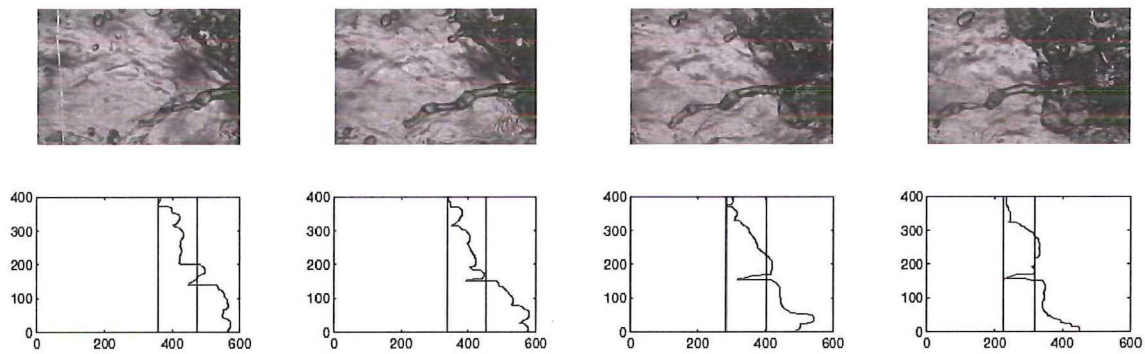
Figure 7.3: Original pictures of a proceeding roll wave and the contour plots of the same roll wave, the time between each picture is 1 ms. In the contour plots, there are two vertical lines, the left line is the front position of the roll-wave contour and the right line is the average position of the roll-wave contour. The positions of the front and the average position of the roll-wave contour are followed in time to find the velocity. The numbers on the axes are the pixel positions in the picture.

7.2.2   Length

From the movies, an estimate can be made of the length of the roll waves. The roll-wave length is defined as the distance between the front and the back of a roll wave, this is illustrated in figure 7.2. In the literature, several references are present on the roll-wave lengths in horizontal annular flow, like Paras et al. [26] and Belt [6].

The view in which the roll waves are examined is only 32 mm wide, and since some of the roll waves are longer than that (up to 200 mm) it often happens that the roll wave spans several frames. To cover for this, the roll wave needs to be examined carefully: The flow is from right to left and when the first point arrives in which the roll wave spans the hole view, a snapshot is made. Then the movie is played further and a snapshot is made when the most right structure from the first snapshot just leaves the view. This is repeated until the roll wave has passed by; the number of snap shots is multiplied by 32 mm and the total roll-wave length comes out.

Since the roll-wave structure changes during the passage of the camera, there is a source of error in this way of determining the roll-wave length, this error is estimated to be around 15 %. Also the determination of the front and the back of the roll wave is a source of error, since the front and the back of the roll wave are not well determined. There is always some sort of deformation in the front of the roll wave from which it is hard to determine the actual front, this leaves some arbitrariness in the determination of the edge of the roll wave. This gives an error of around 5 %.

7.2.3   Frequency

When a roll wave passes, the light that passes through the liquid film is reduced. The droplets in the roll wave scatter the light such that it isn't seen by the CMOS sensor so the average light intensity on the pictures decreases. With information of the mean intensity of the light in the pixels in a picture a measure of the frequency of the roll waves is possible. When the intensity in the picture drops, the arrival of a roll wave is indicated. The pixel intensity is a value between 0 and 255, where a pixel with a value of 0 means that the pixel is black and a value of 255 means the pixel is white.
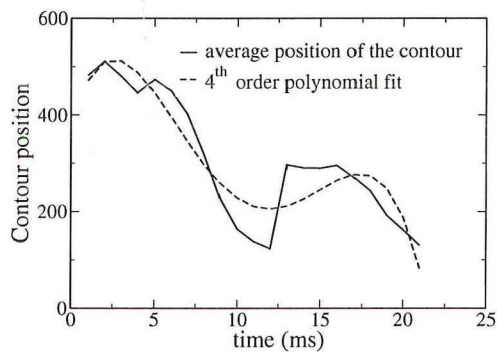
Figure 7.4: Plot of the mean position of a contour in time. A 4th order polynomial fit is used to find the time it takes for a roll wave to pass the field of view. This time is taken to be the difference between the local maximum on the left (t = 3 ms) and the local minimum at the centre (t = 12 ms), the velocity is then determined as $v = \frac{\Delta x}{\Delta t}$.
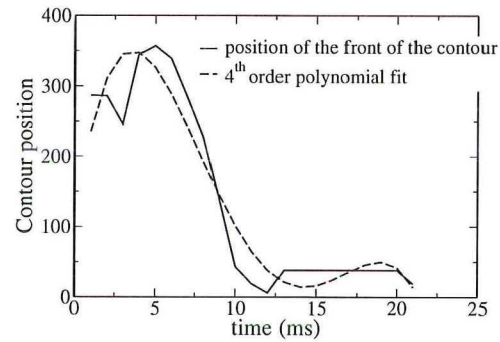
Figure 7.5: Here a plot of the front position of the same contour as in figure 7.4 is shown. The time difference between the maximum on the left and the local minimum in the centre of the plot is a bit different from the mean position of the contour. If the difference is not too large, the time differences are averaged and the reported velocity is the mean velocity of the front position and the mean position of the roll wave.

With Matlab all the frames in a movie are processed and the mean intensity of all the frames is calculated, this is called the total mean intensity. Also the standard deviation of the total mean intensity is calculated. After that the mean intensities of the pixels per frame are calculated. The mean intensity per frame is subtracted from the total mean intensity and when the difference is larger than the standard deviation, the frame is considered to be part of a roll wave. The plot of this is given in figure 7.6 and 7.7. The results for the frequencies are compared to the images of the actual roll waves passing by. It is seen that there is some uncertainty in the values of the frequencies. The roll waves can consist of two parts, separated by a lighter region, this causes a single roll wave to be counted as two roll waves. It is also possible that two roll waves are close to each other and counted as one. These kind of errors accumulate to an uncertainty of 5 % in the values of the frequencies.

7.3   Results

7.3.1   Roll-wave velocity

In analysing the roll-wave velocity, for each combination of u_{sl} and u_{sg}, fifteen roll waves were analysed and the average values of the velocities were determined. The results for the average roll-wave velocities are summarised in figures 7.8 and 7.9. It is seen that the roll-wave velocity grows with superficial gas velocity, but hardly with superficial liquid velocity. The average roll-wave velocity and statistical uncertainties follow from the relationship in equation 6.1 and 6.2, where u_{ripple} is replaced by u_w.

Results of the Matlab routine are given in figures 7.10 and 7.11. In the figures, the results from the Matlab routine are compared to the on sight results given in figure 7.8 for superficial gas velocities of 22 and 30 m/s. The results for u_{sg} = 22 m/s are in good agreement with each other, however the results for u_{sg} = 30 m/s show differences up to 50 %.

Results are shown for low liquid superficial velocities, since these pictures are very sharp.

With these pictures a contour can be well defined and so the determination of the position is quite accurate. With higher liquid velocities and also higher gas velocities, the images become more fuzzy and the contour determination becomes a hard task. The quality of the images can be improved by using a higher frame rate for the camera or by using a shorter shutter time.

7.3.2   Roll-wave length

In this study, the roll-wave length was determined from the movies, made with the high speed camera. The images were examined on sight and for various combinations of u_{sl} and u_{sg}, 20 different roll waves were considered. Distributions of the roll-wave lengths are made and a plot of the average roll-wave length versus u_{sl} and u_{sg} was made. The plots of the average roll-wave lengths versus the superficial gas and liquid velocity are shown in figures 7.12 and 7.13.

From the figures it is seen that the roll-wave length decreases with increasing gas velocity and it increases with increasing the liquid velocity.

The data points, shown in figures 7.12 and 7.13 are average values of measurements on twenty roll waves. In these measurements a spread is seen in the length of the different roll waves. The distributions of the roll-wave lengths are shown in figures 7.14 and 7.15. From the distributions, the same trends are seen as in figures 7.12 and 7.13. With a growing superficial gas velocity, the roll-wave length decreases. Also the broadness of the distribution decreases with increasing gas velocity.

With growing superficial liquid velocity, also the amount of large roll waves grows. This means a broader distribution of the roll-wave lengths when the liquid flow is higher.

From the repeated measurements, the average roll-wave length and the statistical uncertainty are calculated, using equations 6.1 and 6.2 with u_{ripple} replaced by L_w.
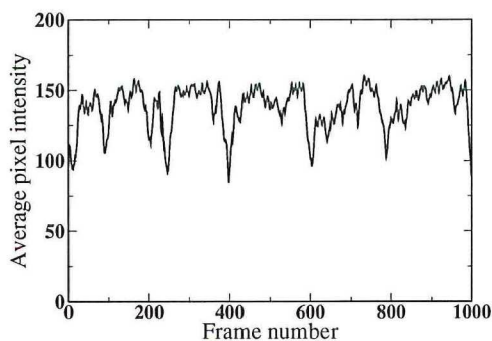
Figure 7.6: Measure of the mean intensity of the pixels per frame for a liquid superficial velocity of 3 cm/s and a gas superficial velocity of 22 m/s. The measurement time is 1000 ms.
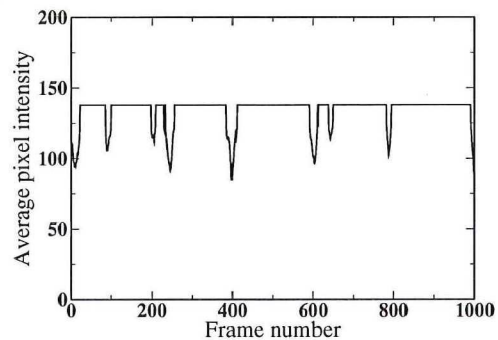
Figure 7.7: Here the standard deviation of the intensity is subtracted from the mean intensity. Every frame with an intensity lower than the mean minus the standard deviation is displayed as a peak below the mean value. These peaks correspond to the roll waves.
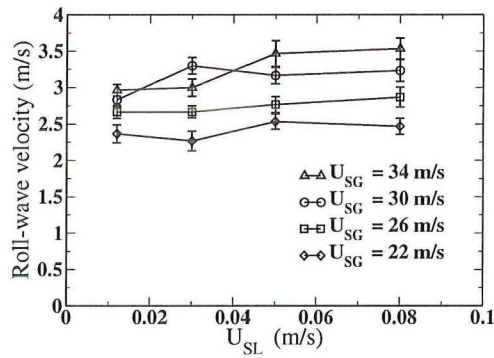
Figure 7.8: Plot of roll-wave velocities at different gas and liquid superficial velocities.
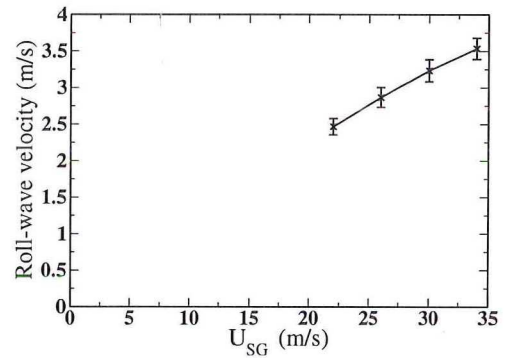

Figure 7.9: Roll wave velocity at a superficial liquid velocity of 8 cm/s versus the superficial gas velocity.
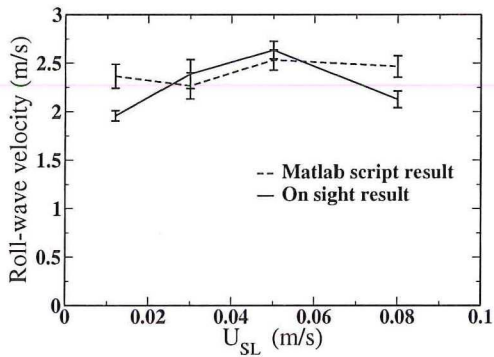

Figure 7.10: Average velocity results, using the Matlab routine, compared with the on sight results for $u_{sg} = 22$ m/s.
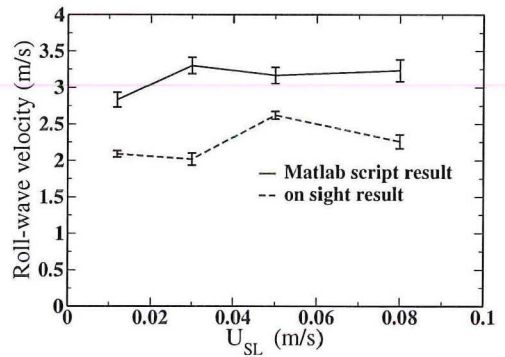

Figure 7.11: Average velocity results, using the Matlab routine, compared with the on sight results for $u_{sg} = 30$ m/s.

Figure 7.12: Plot of the mean roll-wave length versus the superficial liquid velocity with a superficial gas velocity of 22 m/s. The error bars represent the statistical uncertainty, following from equation 6.2.

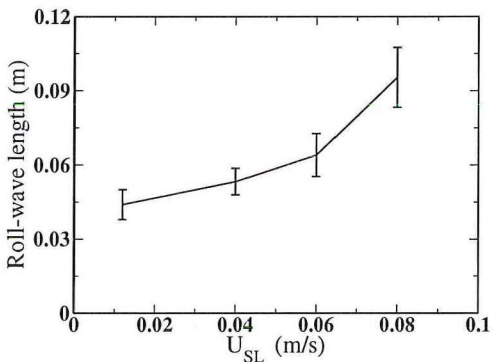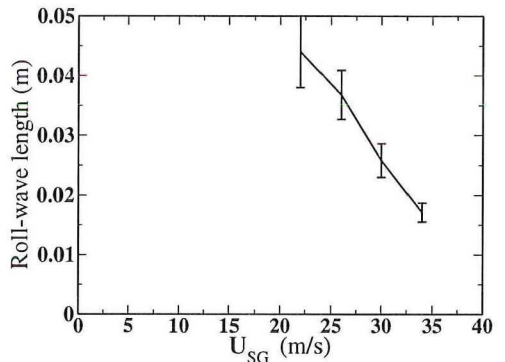**Figure 7.13:** Plot of the mean roll-wave length versus the superficial gas velocity with a superficial liquid velocity of 1.2 cm/s. The error bars represent the statistical uncertainty, following from equation 6.2.

7.3.3 Roll-wave frequency

The frequency measurements of several combinations of superficial gas and liquid velocities are examined, the resulting frequency plot are given in figure 7.16.
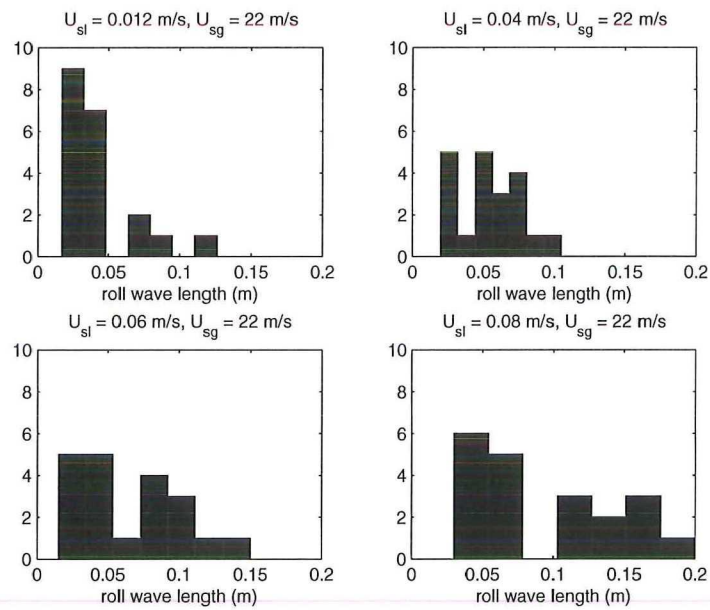
Figure 7.14: Distributions of the roll-wave length for flows with a constant superficial gas velocity of 22 m/s. Superficial liquid velocities are 1.2, 3, 6 and 8 cm/s.
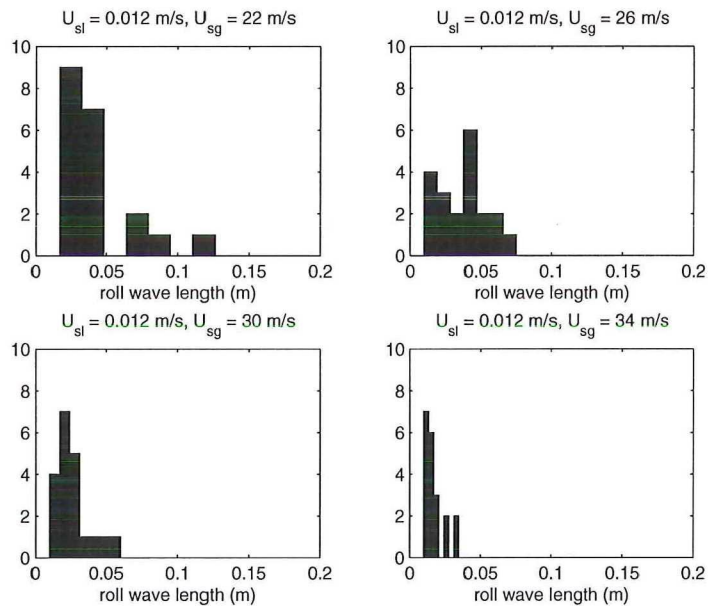
Figure 7.15: Distributions of the roll-wave length for flows with a constant superficial liquid velocity of 1.2 m/s. Superficial gas velocities are 22, 26, 30 and 34 m/s.

Figure 7.16 shows that the roll-wave frequency strongly depends on the superficial gas velocity but hardly on the superficial liquid velocity. In figure 7.17 the average roll-wave frequency per superficial gas velocity is shown. It is seen that the roll-wave frequency grows with superficial gas velocity, but no conclusions can be drawn on the relation since
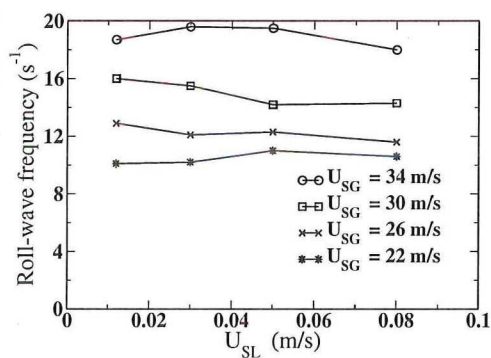
Figure 7.16: Plot of the frequencies of the roll waves at different superficial velocities. The data are averaged values of two samples of 4.473 seconds (4,473 frames).
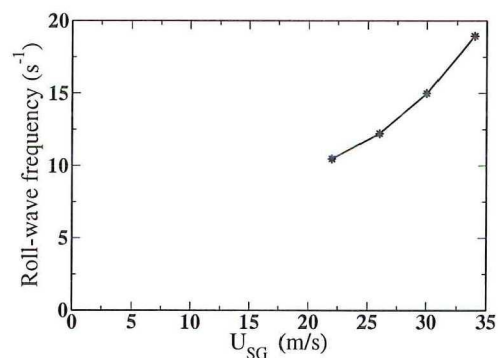
Figure 7.17: Average roll-wave frequency versus superficial gas velocity. The roll-wave frequency grows strongly with superficial gas velocity.

only 4 data points are considered.

7.4   Comparison with the literature

In the literature, Paras et al. [26] provide experimental data on frequency, velocity and length of large roll waves in horizontal annular flows. In their set-up, a pipe is used with an inner diameter of 50.8 mm, comparable to the pipe in the present investigation. Measurements are done on annular flows with superficial gas velocities of 30 m/s and higher. In our experiments, sets of data are available with superficial gas velocities of 30 m/s and 34 m/s, so our data can be compared to the data by Paras et al. Comparative plot of these data are given in figures 7.18 to 7.21.

Comparing the different data from Paras et al. to the data found in the current work, we see that there is a large difference between the values found in their experiments and the values from the present investigation. Figures 7.18 to 7.20 show that our roll-wave length is much lower than the lengths found by Paras, while the velocities and frequencies are much higher.

The lower roll-wave length and higher roll-wave frequency are expected from the differences in the measurements. Paras et al. consider only large roll-waves, while in the present measurements all the roll waves are regarded. This means that the average roll-wave length is lower and the frequency higher.

The qualitative behaviour of the roll-wave length and frequency are the same, compared to Paras et al. When the superficial liquid velocity increases, the roll-wave length increases and the roll-wave frequency decreases.

The general behaviour of the roll-wave velocity is also the same for Paras et al. and the present study. When the superficial gas velocity increases, the roll-wave velocity also increases. The roll-wave velocities from the present study lie almost twice as high as the velocities found by Paras et al. This might have to do with the fact that they only considers large roll-waves; maybe larger roll waves move with a lower velocity than small roll waves.

A quantity used by Paras et al. [26] to estimate the time a roll wave is present, is the wave

intermittency. The wave intermittency is defined as:

$$INT = \frac{f_w L_w}{v_w} \tag{7.1}$$

The wave intermittency represents the fraction of time a roll wave is present. In figure 7.21, the intermittencies found by Paras et al. are compared to the intermittencies found in this report. For low superficial liquid velocities, the intermittencies differ a lot, but for the higher superficial liquid velocities, they are comparable.
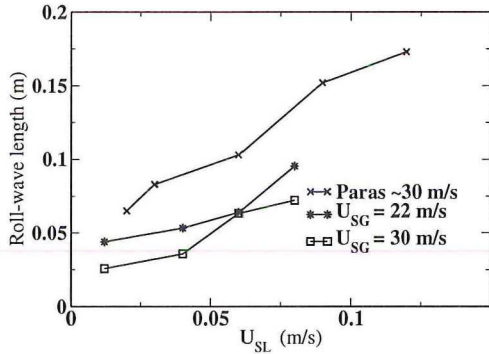
Figure 7.18: Plot of roll-wave lengths for superficial gas velocities of 22 m/s and 30 m/s, compared with the data from Paras et al. [26].
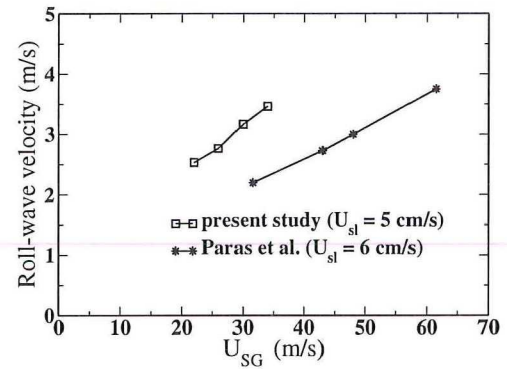
Figure 7.19: Comparison between the roll-wave velocities found by Paras et al.[26] and results from the present investigation.
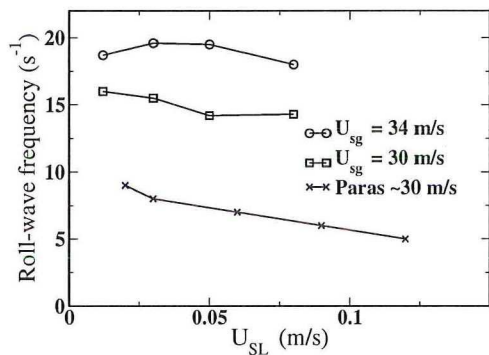
Figure 7.20: Comparison between the roll-wave frequencies found by Paras et al.[26] and results from the present investigation.
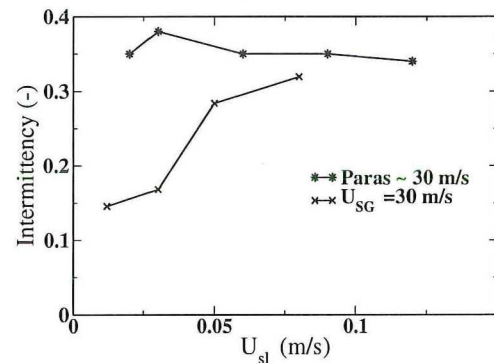
Figure 7.21: Comparison between the roll-wave intermittencies found by Paras et al.[26] and results from the present investigation.

Chapter 8

Droplet entrainment due to roll waves

The droplet size distributions above the roll waves are estimated from the pictures of the roll waves. This gives data in another region in the flow, than data reported by van 't Westende [32]. In the work of van 't Westende the liquid film was sucked from the flow and measurements were done on the droplet velocity and size distribution in the gas core. The reported droplet sizes in the gas core are for vertical flows. The average droplet sizes are 100 to 200 μm for superficial liquid velocities of 20 to 40 m/s. The largest droplets found, are around 750 μm in diameter.

In order to suck away the liquid film, van 't Westende implemented a porous wall and a slit. In this way the total diameter of the pipe was reduced to 40 mm, so a liquid film with a maximum thickness of 5 mm was sucked away. In the work from Belt [6], data are reported on the liquid film thickness in horizontal annular flow. At the bottom of the pipe, mean film thicknesses of 300 to 900 μm are reported. The superficial gas velocities range from 26 to 41 m/s and a superficial liquid velocity of 0.02 m/s.

In the present work, the liquid surface and the region just above it are examined with a field of depth of approximately 5 mm. The results from the present investigation complement the study done by van 't Westende [32], since van 't Westende did his measurements on entrainment further away from the liquid film.

8.1 Droplet entrainment in roll waves

Estimates of the amount of liquid entrained above a roll wave are made, from the pictures of the roll waves. Due to the complexity of the roll waves, an automated analysis, based on image analysis, lies outside the scope of this project. To give an idea of possibilities of the analysis of roll waves, for two gas/liquid flow rates, four roll waves are examined. From the pictures of the roll waves, the amount of droplets was determined and the Sauter mean diameter was estimated. Using the droplet sizes, the amount of entrained liquid on top of a roll wave was estimated. To detect droplets in the roll wave, the picture of the droplet should be at least three pixels wide. The spatial resolution in the pictures is 40 μm per pixel, so droplets with a diameter smaller than 120 μm are not detected. The measure of uncertainty is two to three pixels, so 80 to 120 μm. Results for the two gas/liquid flow rates are summarised in table 8.1.

Table 8.1: Characteristics of droplets on top of roll waves for two gas/liquid flow rates

Roll wave number	$u_{sl} = 1.2 cm/s$ and $u_{sg} = 22 m/s$			$u_{sl} = 1.2 cm/s$ and $u_{sg} = 30 m/s$		
	Average droplet diameter (μm)	Number of droplets	Total entrained liquid volume (m^3)	Average droplet diameter (μm)	Number of droplets	Total entrained liquid volume (m^3)
1	300	47	$0.7 \cdot 10^{-9}$	418	159	$6.0 \cdot 10^{-9}$
2	477	93	$5.3 \cdot 10^{-9}$	403	116	$4.0 \cdot 10^{-9}$
3	590	118	$1.0 \cdot 10^{-8}$	348	112	$2.6 \cdot 10^{-9}$
4	567	151	$1.4 \cdot 10^{-8}$	396	136	$4.4 \cdot 10^{-9}$
average	484	102	$7.5 \cdot 10^{-9}$	391	131	$4.3 \cdot 10^{-9}$
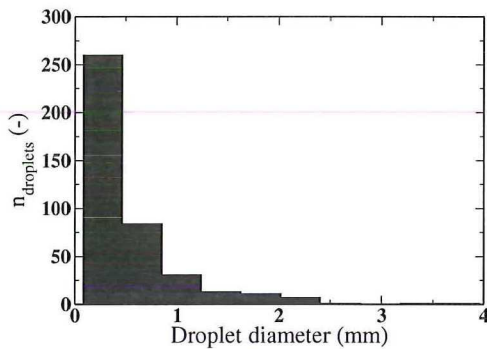
Figure 8.1: Distribution of droplet diameters in four roll waves in horizontal annular flow with a superficial liquid velocity of 1.2 cm/s and a superficial gas velocity of 22 m/s. Note that there are two droplets larger than 3 mm in the sample.
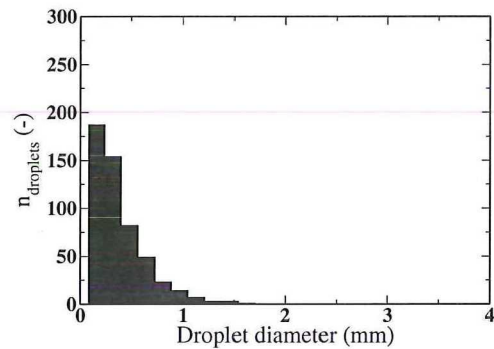
Figure 8.2: Distribution of droplet diameters in four roll waves in horizontal annular flow with a superficial liquid velocity of 1.2 cm/s and a superficial gas velocity of 30 m/s. The maximum droplet size in this sample is about 1.7 mm.

As can be seen in table 8.1, there are a lot of droplets present in a single roll-wave. For the four roll waves per u_{sg}/u_{sl} combination, the total size distributions are shown in figures 8.1 and 8.2. The droplet diameter distributions are roughly the same, only in the case with $u_{sg} = 22$ m/s the tail of the distribution is much longer. The largest droplets from the roll waves have a diameter of 4 mm, which is much larger than reported by van 't Westende [32]. The sizes of the largest droplets also get much closer to the maximum droplet diameter predicted by Turner (section 2.3) of 8.5 mm.

In the $u_{sg} = 30$ m/s case, the tail of the distribution is shorter, but a significant amount of droplets has a diameter of 1 mm or more. This is much larger than reported in literature; see for instance Hay et al. [14] or van 't Westende [32].

8.2 Total droplet entrainment

The total amount of entrainment is not detectable using the present method. With the current measurement set-up, only an estimate of the total amount of entrained liquid in the roll waves can be given. For the total amount of entrainment in the roll waves, several other quantities need to be measured, such as the roll-wave frequency, the average roll-

wave length and the average roll-wave velocity. These quantities, give a measure of the amount of surface which is covered with roll waves and are reported in chapter 7.

The data in table 8.1 is given for roll waves of approximately 3 cm in length, from this the amount of entrained liquid per unit of roll-wave length, 'E_l', is estimated. The total amount of entrained liquid in roll waves passing by per unit of time is:

$$E_t = E_l \cdot < L_w > \cdot f_w \tag{8.1}$$

with $< L_w >$ being the average roll-wave length and f_w is the roll-wave frequency.

With a typical value of the roll-wave frequency of 15 s^{-1} (section 7.3.3) and a typical roll-wave length of 2.5 cm (section 7.3.2), the amount of liquid entrained in roll waves adds up to $5 \cdot 10^{-5}$ kg/s. With a superficial liquid velocity of 1.2 cm/s, a total mass flow rate of 0.024 kg/s is encountered, so the fraction of liquid entrained just above the liquid surface of the roll waves is approximately 0.2 % of the total liquid flow.

Void fraction

From the data from van 't Westende [32], the void fraction of the droplets in the gas core, α_{dr} for a flow with $u_{sl} = 1$ cm/s and $u_{sg} = 21$ m/s, is $\alpha_{dr} = 0.5 \cdot 10^{-4}$ m^3/m^3. With the data from table 8.1 the void fraction of the droplets in the roll waves is determined, which can be expressed as follows:

$$\alpha_{dr,wave} = \frac{E}{L_w \cdot W \cdot H} \tag{8.2}$$

The focal field of depth of the camera is around 4 mm, so this is a measure for the thickness, H, of the roll wave. The roll waves examined are about 3 cm long (L_w) and 2.4 cm wide (W). For the total void fraction due to the roll waves, the following expression is used:

$$\alpha_{dr,wave} = \frac{E}{\pi \cdot r^2 \cdot \frac{L_w}{INT}} \tag{8.3}$$

Here, r is the radius of the pipe and INT is the intermittency.

In table 8.1 it is seen that the average amount of liquid entrained is 10^{-8} m^3, so the void fraction in the roll wave is around 1%. With this void fraction, the liquid mass fraction in this area is calculated to be 10 kg/m^3. This result suggests that two-way coupling effects between tha gas and the liquid have to be considered in this region of the flow.

For the void fraction due to the roll waves in the whole pipe, the data on the intermittency is needed. In figure 7.21 typical values for the intermittency are found of 0.15 to 0.35. Taking a value of 0.25 for the intermittency, this gives a void fraction due to the roll waves of $0.5 \cdot 10^{-4}$ m^3/m^3. The void fraction found in the core by van 't Westende is $0.5 \cdot 10^{-4}$ m^3/m^3, so the void fraction due to the roll waves is a significant part of the total entrainment and should be taken into account.

In the analysis given above, it should be pointed out that this is an estimate of the order of magnitude of the droplet entrainment. The numbers which are given show that the amount of entrainment on top of a roll wave is in the same order of magnitude as the amount of entrainment in the gas core, so it should be taken into account. The investigation was on a small sample, so the uncertainty in the values is large. From a statistical point of view, using equation 6.2 with u_{ripple} replaced by the total droplet entrainment, uncertainties of 20 and 40 % are found in the total entrained liquid volume.

8.3   Ligaments in roll waves

In the roll waves, also liquid ligaments are present. Ligaments are elongated chunks of liquid which form from the liquid film due to the high gas velocity. The ligaments break-up in the gas stream and form droplets of different sizes. The pictures of the annular flows show examples of these ligaments.

In the snapshots of the flow, a small amount of ligaments is visible. Due to the rapid movement of the liquid film, these ligaments exist for a short amount of time, typically about 3 to 5 milliseconds. This means that the amount of liquid 'entrained' in the ligaments is changing all the time, while the total amount of liquid entrained in the droplets is roughly constant. Data on the amount of ligaments and the amount of liquid in them is given in table 8.2. The size of a ligament is estimated by imposing a cylinder with the length and width of the ligament. The roll-wave numbers in table 8.2 correspond to the same roll waves as in table 8.1.

Table 8.2: Characteristics of ligaments in roll waves for two combinations of u_{sl} and u_{sg}

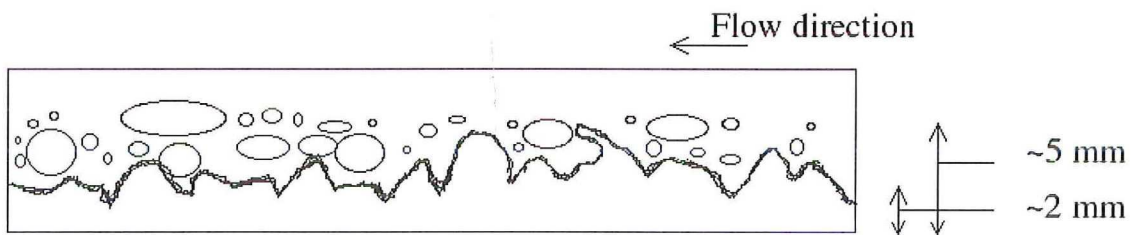| Roll wave number	$u_{sl} = 1.2cm/s$ and $u_{sg} = 22m/s$		$u_{sl} = 1.2cm/s$ and $u_{sg} = 30m/s$	
	Number of ligaments	Total liquid volume in the ligaments (m^3)	number of ligaments	Total liquid volume in the ligaments (m^3)
1	4	$5.8 \cdot 10^{-10}$	3	$2.7 \cdot 10^{-10}$
2	3	$1.9 \cdot 10^{-10}$	3	$8.6 \cdot 10^{-11}$
3	1	$3.3 \cdot 10^{-11}$	5	$1.8 \cdot 10^{-10}$
4	3	$8.1 \cdot 10^{-10}$	4	$4.4 \cdot 10^{-10}$

When the values of the droplet entrainment in table 8.1 are compared to the values of the entrainment of water due to ligaments in table 8.2, it is seen that the amount of entrainment due to droplets is much larger. The explanation for this is that the ligaments only exist for a short period of time, before they break up into droplets. The droplets from the ligaments stay on top of the roll wave for a much longer period of time.

8.4   Roll-wave final view

The movies and the data on the roll waves, give an impression of how the roll waves behave in annular flow. In figure 7.2 a schematic view of what a roll wave looks like is given, but with the data in this chapter this impression can be extended.

In figure 8.3 a schematic view of an intersection of a roll wave is presented based on the droplet data in this chapter and data of Belt [6]. Belt states that the roll-wave film-height is about 1 to 2 mm. The camera is focused just above the liquid film, such that the roll waves are in focus. The field of depth is about 4 mm, so the assumption is made that the droplets are at a maximum height of 5 mm. The liquid hold-up in this region is about 1 % and every once in a while a ligament shows up, which breaks up into droplets.

In figures 8.4 and 8.5, two pictures are shown of small roll waves with ligaments and droplets with diameters ranging from 120 to 2500 μm. These pictures confirm the view sketched in figure 8.3. The larger droplets seem to be elongated in the direction of the

Figure 8.3: Schematic view of an intersection of a roll wave, the average film height is around 2 mm and the droplets in the roll wave reach a maximum height of 5 mm. The maximum droplet diameter is around 4 mm for flows with $u_{sl} = 1.2 cm/s$ and $u_{sg} = 22 m/s$.

flow, which is also depicted in figure 8.3. The pictures have been manipulated with some brightening and contrasting tools to improve the visibility of the ligaments and droplets. The dark spots in the corners of the pictures are caused by the window through which the flow is being recorded.
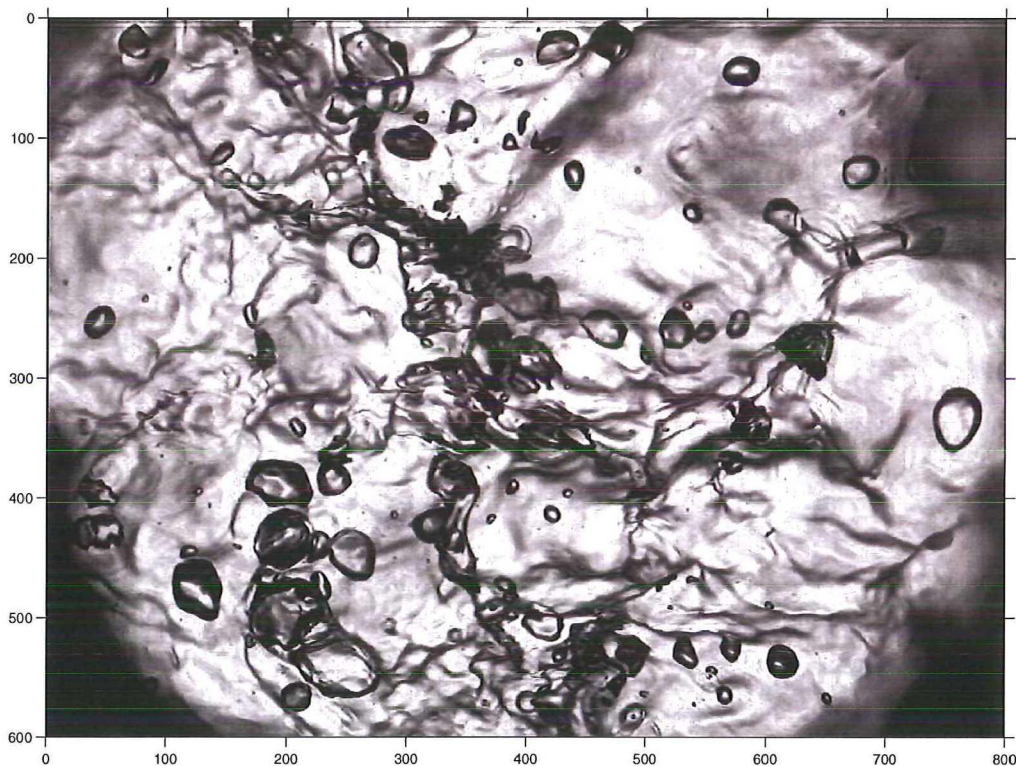
Figure 8.4: Picture of a small roll wave in an horizontal annular flow with $u_{sl} = 1.2 cm/s$ and $u_{sg} = 22 m/s$. On the axes, the number of pixels is displayed, and 1 pixel corresponds to 40 μm. In the region with the values on the x-axis ranging from 100 to 300 and values on the y-axis ranging from 380 to 580, droplets are visible with diameters of 1.5 to 2.5 mm. An example of a ligament is starting at (x,y) = (250,180) and ending at (150,150). Note that the values on the y-axis start with 0 on top and end with 600 at the bottom. The direction of the flow is from right to left.
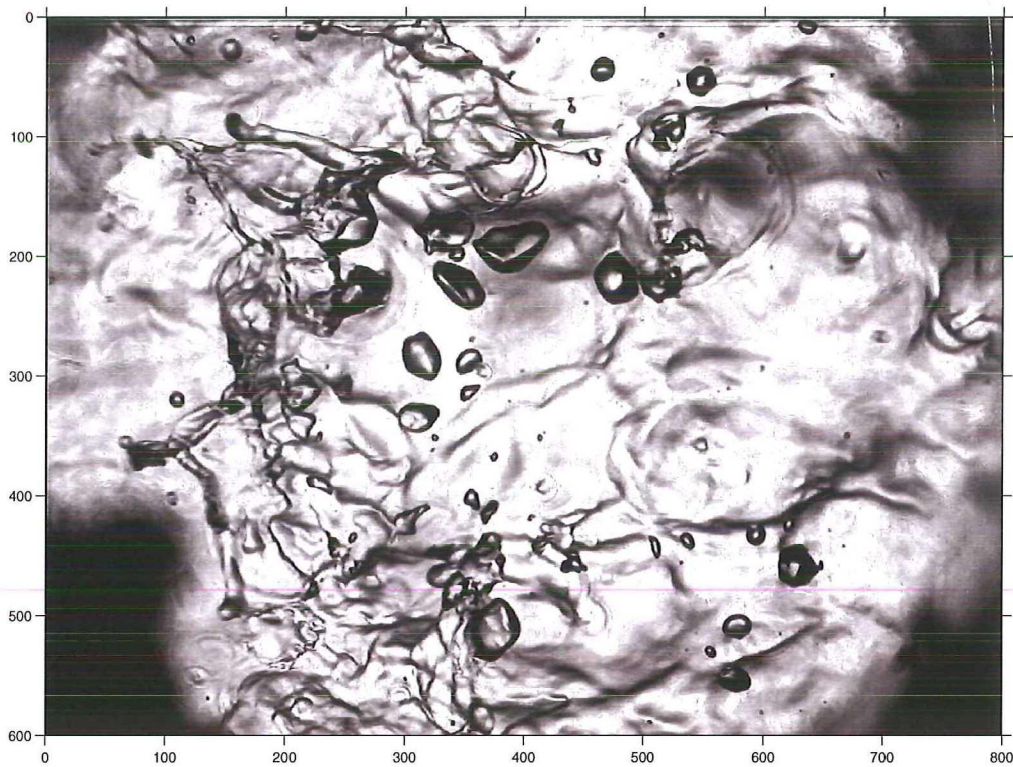
Figure 8.5: Here another small roll-wave is shown. Some examples of ligaments can be found at (x,y) = (250,100) to (150,100) and at (100,380). An example of a large droplet is seen at (400,200). The direction of the flow is from right to left. The velocities are: $u_{sl} = 1.2 cm/s$ and $u_{sg} = 22 m/s$.

8.5   Discussion

In this thesis, maximum droplet diameters are found for flows with u_{sl} = 1.2 cm/s and u_{sg} = 22 m/s, which have a maximum droplet diameter of 4.0 mm. In flows with u_{sl} = 1.2 cm/s and u_{sg} = 30 m/s a maximum droplet diameter of 1.7 mm is found.

In the theory about the maximum droplet sizes in annular flow, values of 1 to 2 mm are predicted for the maximum droplet diameter from the analysis of Kocamustafaogullari [21], section 2.3. The analysis of Kocamustafaogullari takes into account the eddies from the turbulent flow to predict the maximum droplet size. Compared to the work of van 'Westende [32] it is seen that Kocamustafaogullari's approach gives values within a factor of two for the maximum droplet diameter in the gas core of an annular flow. The results in this chapter show that the predictions from this approach do not hold in the region just above the liquid layer.

In the industry, the criterion proposed by Turner [30] is used to predict the onset of liquid loading. The Turner criterion is based on a balance between the average drag force and the surface tension for a droplet pending in a uniform gas flow. The superficial gas velocity predicted for the onset of liquid loading is 14.5 m/s and this corresponds very well to the experimental observations. The maximum droplet diameters predicted at this superficial gas velocity are 8.5 mm, but the droplet sizes do not correspond to the sizes

of the droplets entrained in the gas core that are found in the experiments. The data from van 't Westende for the maximum droplet diameters in the gas core lie more then a factor of ten below the value predicted by Turner.

The droplets observed near the liquid layer are far smaller than the largest droplets predicted by the Turner criterion. However, the maximum droplet diameters from the Turner criterion were predicted for droplets pending in a uniform flow with a gas velocity of 14.5 m/s. This means that the relative velocity of the droplets compared to the gas velocity is 14.5 m/s. In the experiments done here, another relative velocity is applied. As mentioned above, a case with $u_{sg} = 22$ m/s and a case with $u_{sg} = 30$ m/s are examined. At these superficial gas velocities, roll-wave velocities of 2.3 and 2.8 m/s are reported in section 7.3. The droplets move with the roll waves, so the assumption is made that the droplet velocities are the same. The relative velocities are 19.7 m/s and 27.2 m/s. The Turner criterion was defined as:

$$We_{crit} = \frac{\rho_g u_{dr,t,max}^2 d_{dr,max}}{\sigma} = 30 \tag{8.4}$$

When the values for the relative velocities of 19.7 and 27.2 m/s are filled in in this criterion, maximum droplet diameters of 4.7 and 2.4 mm come out. These values lie close to the values found in the determination of the droplet sizes of 4.0 and 1.7 mm.

8.6   Conclusion

Until now it was not clear why the Turner criterion predicted the onset of liquid loading very well, while droplets of the size predicted by the Turner criterion were not observed. In the measurements done here, droplets are observed that satisfy the Turner criterion for the maximum droplet size. The largest droplets are found in the near wall region and not in the gas core. Up to now no detailed measurements have been done in the near-wall region. The results give a validation of why the Turner criterion works well.
The fact that the large droplets are in the near-wall region suggests that the onset of liquid loading occurs in this region and not in the gas core. The large droplets fall back in the liquid film, with a momentum exchange in the direction opposite to the gas flow direction, pushing back the liquid.

Chapter 9

Conclusions and recommendations

9.1 Conclusions

In this work the possibilities of the use of a high-speed camera in the study of annular flows was investigated. First of all, we wanted to know if it is possible to use a high speed camera for the visualisation of the liquid film in annular flow. Then we wanted to know what the possibilities are for such a set up.

To investigate the use of a high speed camera in this field of work, a running set up was created. The flow pipe used at the Kramerslab was adjusted with a hole in the pipe through which the liquid surface can be filmed. The results show a good visualisation of the liquid topology for stratified and annular flow patterns. On sight analysis of the pictures by hand gives good results, but the implementation is a bit arbitrary and is very time consuming. Different automation methods were tried and implemented that show promising results. Further work on this is required involving signal analysis and pattern recognition.

In the annular flows, the ripple-wave pattern was investigated by hand, and data on the ripple-wave orientation and velocity is obtained. The orientation of the ripples was expected to be symmetrical, with the length of the bottom of the pipe as the axis of symmetry. The results from the picture analysis confirm this assumption, but only a small amount of pictures has been examined. The ripple-wave velocity was also investigated by hand and it was seen that the ripple-wave velocities lie between 0.9 and 1.6 m/s. The ripple-wave velocities grow with increasing superficial gas velocity.

Also, the roll-wave part of the annular flow was investigated and results are reported on roll-wave frequency, velocity and length. For the frequency and the velocity a Matlab routine has been written to automate the process of image analysis. An attempt was made to automate the analysis of the roll-wave length as well, but this did not give completely satisfactory results so far.
For the roll-wave frequency, we can conclude that the frequency grows with growing superficial gas velocity, but hardly with superficial liquid velocity. The roll-wave frequencies lie in a range of 10 to 20 roll waves per second for superficial gas velocities of 22 to 34 m/s.
For the roll-wave velocity we see that the velocity grows with increasing superficial gas velocity but there is no dependency on the superficial liquid velocity. The roll-wave velocities lie between 2 and 4 m/s, this is 2 to 3 times the ripple-wave velocity.

The roll-wave length was examined on sight, this length depends on both the superficial gas and liquid velocities. For high superficial gas velocities and low superficial liquid velocities the roll waves are on average 2 cm long while for a low superficial gas velocity and a high superficial liquid velocity roll-wave lengths grow to 10 cm (twice the pipe diameter).

In the analysis of the roll waves, also the structure of the roll waves was taken into account. In the literature, the image is sketched that the roll waves exist of several wavelets on top of the liquid film, but attached to the liquid film. What is shown in this work is that a roll wave consist of a large coherent structure, with lots of droplets and ligaments, travelling above a rippled liquid surface.
The maximum droplet diameters are well predicted by the Turner criterion and this gives a confirmation of the use of the Turner criterion. The Turner criterion is often used in the industry to predict the onset of liquid loading, but the predicted maximum droplet diameters were not observed in experiments. In our experiments large droplets with diameters close to the predicted values from Turner are observed. These droplets are found in the region near the liquid surface.
The observation that the large droplets are in the region near the liquid film, suggests that the liquid loading starts in this region and not in the gas core.

9.2   Recommendations

In this report, some interesting results are shown from measurements with a high speed camera on stratified and annular flow. This work has been the first of its kind at the Kramers laboratory, so there is a lot of space for future investigation using a high-speed camera.

We have seen that there is a possibility of setting up an onset of entrainment chart for the flow loop in use. This chart can be expanded for several orientations of the flow pipe.

The subject of ripple-wave analysis can be expanded by investigating the use of image analysis software on the pictures of the flow. With this kind of software it might be possible to give a good description of the surface topology. A good description of the surface topology can result in an accurate model for the relative surface roughness due to the liquid layer.
Another way of finding data on the surface roughness is with the use of stereo photography. With this measurement technique it might be possible to find the ripple-wave heights in the liquid layer, this was not possible with the conductance probe measurements by Belt [6] due to a lack of resolution. An introduction on stereo photography is given in appendix B.

In the part of the roll-wave analysis some improvements can be suggested. In the part of the roll-wave length and velocity a zoomed-out view is possible. With this, the spatial resolution will be worse, but roll waves will be captured in a single frame. If the pictures are zoomed out enough, it will even be possible to follow the roll wave through a couple of frames and thus determining the roll-wave velocity. In a measurement like this it is also possible to determine the roll-wave length much easier and the roll-wave lengths can be linked to the roll-wave velocities. A correlation between the roll-wave length and

roll-wave velocity can be investigated in this way. Measurements like this have been done by Schubring et al. [29] on vertical pipe flows and the results look promising.

The entrainment measurements are a significant improvement to existing work. The present set up can be used in combination with the conductance probe from Belt [6] and the PDA measurements of van 't Westende [32]. These combined measurements can return a nice overall view of the behaviour of the liquid film, droplet entrainment and the region in between where the roll waves are present. To improve the results from such a measurement, it might be necessary to use a higher frame rate or a higher spatial resolution. The camera used in this project has the downside that the spatial resolution decreases when the frame rate is increased. To overcome this disadvantage, the use of a camera with a higher spatial resolution should be considered.

In order to give more firm conclusions on the onset of liquid loading, extra measurements should be done with superficial gas velocities around 14.5 m/s. This is the superficial gas velocity at which Turner predicts the onset of liquid loading. Measurements like this should be carried out in a vertical pipe to see if there are droplets pending in the near wall region with diameters up to 8.5 mm. When the superficial liquid velocity is decreased further, droplets should be visible that fall back in the direction opposite to the direction of the gas flow.

Acknowledgements

Bibliography

[1] Andreussi, P. and Azzopardi, B.J. (1983). Droplet deposition and interchange in annular two-phase flow. *Int. J. multiphase flow.*, **9**, 681-695

[2] Asali, J.C. and Hanratty, T.J. (1986). Interfacial Drag and Film Height for Vertical Annular Flow. *AIChE Journal.*, **31**, 895-902

[3] Asali, J.C. and Hanratty, T.J. (1992). Ripples generated on a liquid film at high gas velocities. *Int. J. multiphase flow.*, **19**, 229-243

[4] Azzopardi, B.J. and Teixeira, J.C.F. (1994). Detailed measurements of vertical annular 2-phase flow 1. Drop velocities and sizes. *J. of fluids engineerings-transactions of the ASME.*, **116**, 792-795

[5] Azzopardi, B.J. (1997). Drops in annular two-phase flow. *Int. J. multiphase flow.*, **23**, 1-53

[6] Belt, R.J. (2007). On the liquid film in inclined annular flow. *Ph.D thesis TU Delft.*

[7] Bueren, J.E.P. van (2009). Experimental study of liquid loading in inclined upward annular flow. *BSc thesis TU Delft*

[8] de Bertodano, M., Jan, C. and Beus, S. (1997). Annular flow entrainment rate experiment in a small vertical pipe. *Nuclear Engineering and Design.*, **178**, 61-70

[9] Fore, L.B. and Dukler, A.E. (1995). The distribution of drop size and velocity in gas-liquid annular flow. *Int. J. multiphase flow.*, **21**, 137-149

[10] Fore, L.B. and Dukler, A.E. (1995). Droplet deposition and momentum transfer in annular flow. *AIChE Journal.*, **41**, 2040-2046

[11] Hall-Taylor, N.S. and Hewitt, G.F. (1963). The motion and frequency of large disturbance waves in annular two-phase flow of air-water mixtures. *Chemical Engineering Science.*, **18**, 537-552

[12] Han, H. and Gabriel, K. (2007). A numerical study of entrainment mechanisms in axisymmetric annular gas-liquid flow. *J. of fluids engineering.*, **129**, 293-301

[13] Hay, K.J., Liu, Z.C. and Hanratty, T.J. (1996). Relation of deposition rates to drop size at large concentrations. *Int. J. Multiphase Flow.*, **22**, 829-848

[14] Hay, K.J., Liu, Z.C. and Hanratty, T.J. (1998). A back lighted imaging technique for particle size measurements in two-phase flows. *Experiments in fluids.*, **25**, 226-232

[15] Hewitt, G.F. and Hall-Taylor, N.S. (1970). Annular two-phase flow. *Pergamon press.*

[16] Hidma, A. (2007). Experimental study of the pressure drop and liquid ow reversal in inclined upward annular ow. *BSc thesis TU Delft.*

[17] Hinze, J.O. (1955). Fundamentals of the hydrodynamic mechanism of splitting in dispersion processes. *AIChE Journal.*, **1**, 289-295

[18] Holthuijsen, L.H. (1983). Stereophotography of ocean waves. *Applied Ocean Research.*, **5**, 204-209

[19] Ishii, M. and Grolmes, M.A. (1975). Inception Criteria for Droplet Entrainment In Two-Phase Concurrent Film Flow. *AlChE Journal.*, **21**, 309-318

[20] Kemp, H.K. (2004). Droplet size and velocity measurements in annular flow using phase-Doppler anemometry. *MSc thesis TU Delft.*

[21] Kocamustafaogullari, G., Smits, S. R. and Razi, J. (1993). Maximum and mean droplet sizes in annular two-phase flow. *Int. J. Heat Mass Transfer.*, **37**, 955-965

[22] Lopes, J. C. B., and Dukler, A. E.(1985) Droplet sizes, dynamics and deposition in vertical annular flow. *University of Houston Report.*, **32**, 1500-1515

[23] Marmottant, P. and Villermaux, E. (2003). On spray formation. *J. of fluid mechanics.*, **498**, 73-111

[24] Mugele, R. A. and Evans, H. D. (1951). Droplet size distribution in sprays. *Ind. Engng Chem.*, **43**, 1317-1324

[25] Ohba, K. and Nagae, K. (1992). Characteristics and behaviour of the interfacial wave on the liquid film in a vertically upward air-water two-phase annular flow. *Nuclear engineering and design.*, **141**, 17-25

[26] Paras, S.V. and Karabelas, A.J. (1991). Properties of the liquid layer in horizontal annular flow. *Int. J. multiphase flow.*, **17**, 439-454

[27] Rosin, P. and Rammler, E. (1933). Laws governing the fineness of powdered coal. *J. bzst. Fuel.*, **7**, 29-36

[28] Sawant, P., Ishii, M. and Mori, M. (2008). Droplet entrainment correlation in vertical upward co-current annular two-phase ow. *Nuclear Engineering and Design.*, **238**, 1342-1352

[29] Schubring, D., Schedd, T.A. and Hurlburt, E.T. (2010). Studying disturbance waves in vertical annular flow with high-speed video. *Int. J. multiphase flow.*, , **36**, 385-396

[30] Turner, R. G., Hubbard, M. G. and Dukler, A. E. (1969). Analysis and prediction of minimum flow rate for the continuous removal of liquids from gas wells. *J. of petroleum technology.*, **21**, 1475-1482

[31] Villermaux, E. (2007). Fragmentation. *Annular review of fluid mechanics*, **39**, 419-446

[32] Westende, J.M.C. van 't (2008). Droplets in annular-dispersed gas-liquid pipeflows. *Ph.D thesis TU Delft.*

[33] Wohono, S. and Honnery, D. (2006). High-speed visualisation of primary break-up of an annular liquid sheet. *Experiments in fluids.*, **44**, 451-459

[34] Woodmansee, D.E. and Hanratty, T.J. (1969). Mechanism for the removal of droplets from a liquid surface by a parallel air flow. *Chemical Engineering Science.*, **24**, 299-307

Appendix A

Roll-wave velocity distriutions

In this appendix, the distributions of the roll-wave velocities are shown. In figure A.1 the roll-wave distributions for the on sight results are shown and in figure A.2 the distributions from the Matlab routine are shown.
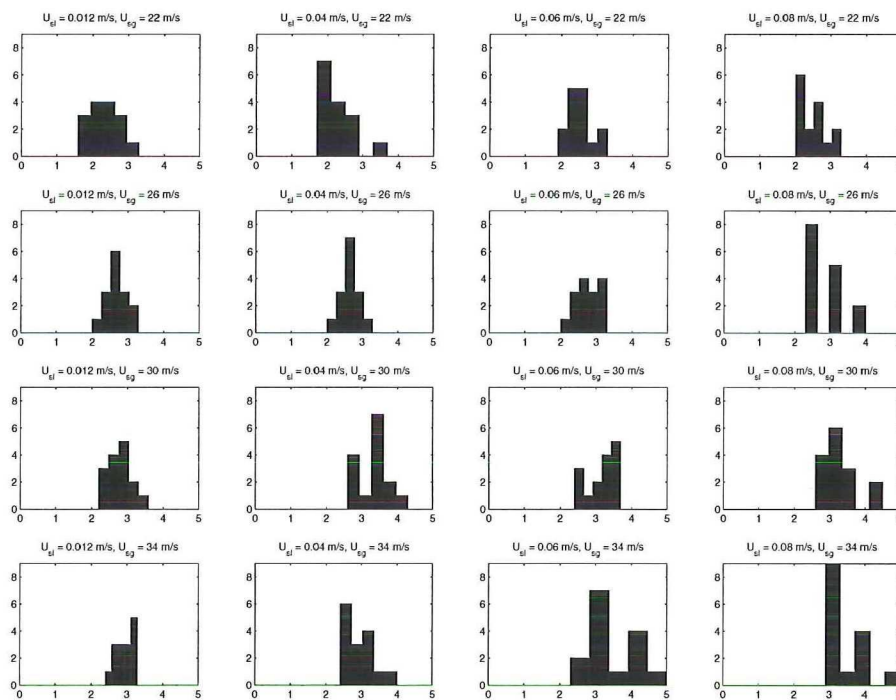
Figure A.1: Distributions of the velocities measured to find the data points in figure 7.8. On the horizontal axes, the roll-wave velocities in m/s are displayed and on the vertical axes the number of the roll waves (n_{waves}) is shown.
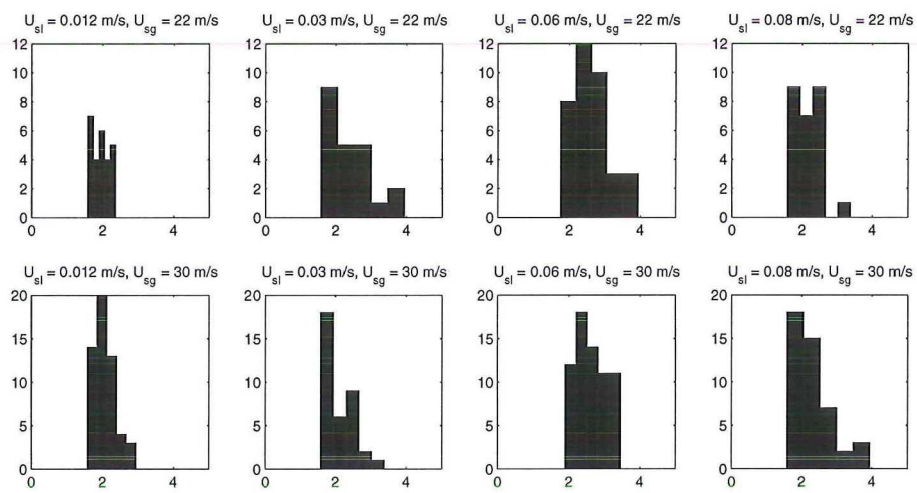
Figure A.2: Distributions of the roll-wave velocities in m/s from the Matlab routine. Two superficial gas velocities are considered: $u_{sg} = 22$ m/s and $u_{sg} = 30$ m/s.

Appendix B

Ripple-wave height determination by use of stereophotography

B.1 Introduction

Stereophotography is a technique used in the determination of ocean-wave heights. An introduction to stereophotography of ocean waves is given in Holthuijsen [18]. Here wind generated waves are discussed, which are wind induced, but Holthuijsen states that stereo photography might be the only technique available to determine the wave height of breaking waves.

The principles of stereophotography seem to apply to the determination of the ripple wave heights in annular two-phase flows. Essentially the problem is the same, since the ripple waves are wind induced waves. Also the comparison of breaking waves from the ocean to the roll waves from the annular flow seems reasonable. So the use of stereo photographic techniques, might give results on the height of the ripple waves and on the 3D structures of the roll waves.

B.2 Theory

In the determination of the geometry of a surface, two pictures can be combined as a stereo photo pair. This is shown in figure B.1, here the point A is projected on two cameras looking downwards. The two cameras are equipped with lenses with the same focal length f and are located at an elevation h_1 with a mutual distance b. When the parallax of the point A is used, the elevation of point A in the surface can be determined. The parallax is given as:

$$p = na_1 - na_1'$$ (B.1)

Where na_1 and na_1' are the abscissas of the projection of A in the left and the right picture respectively, from figure B.1. By the use of similar triangles, it can be shown that the elevation h_2 of point A is:

$$h_2 = h_1 - \frac{bf}{p}$$ (B.2)

This is the basis of the photogrammetric analysis with stereo images.
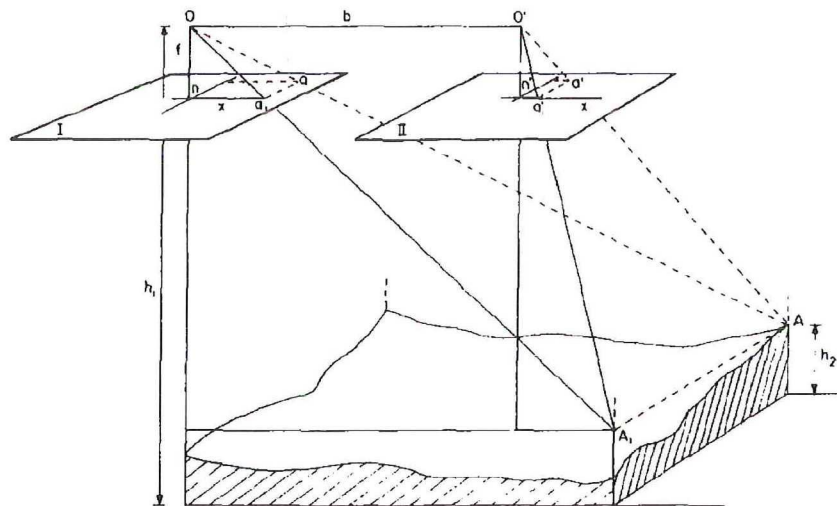
Figure B.1: Projection of a point A in a terrain surface on to the two pictures of a stereo photo pair, from Holthuijsen [18].

Table B.1: Limitations on camera positions and orientations for stereo photography, from Holthuijsen [18].

Altitude difference	< 10% of the total altitude
Overlap of pictures in x-direction	50-70 % of image format in x-direction
Overlap of pictures in y-direction	> 80 % of image format in y-direction
Tilt	< 3°
Difference in orientation	< 15°

B.3   Stereo photography in annular flow

For the use of stereophotography in annular two phase flow, an adjustment of the setup from this thesis is needed. Instead of one camera, two camera's are needed and they need to be carefully aligned. The requirements for a good result are given in the paper by Holthuijsen [18], these requirements are summarised in table B.1.

The limitations given in table B.1 are limitations in the field of ocean wave height determination. This is done using two airplanes flying over the ocean. The use of these two airplanes can cause a large disturbances in the alignment of the cameras. In the controlled environment of the laboratory, the requirements given in table B.1 should be matched relatively easy. A possible setup is given in figure B.2, the cameras can be aligned such that all the requirements from table B.1 will be matched. The assumption is made that the lenses from the cameras have the same focal length.

B.4   Discussion

When stereo photography is used in to determine the ripple wave height in annular flow, a couple of things should be kept in mind. First of all: the distance between the cameras

should be such that the overlap of the pictures is sufficient. Then, thoughts should be spent on the way in which the flow is visualised, i.e. is it necessary to make two holes in the pipe like in figure B.2, or is it better to make one larger hole, through which the two cameras can visualise the liquid layer. By using different kinds of configurations, the flow will be affected in different ways and this should be examined.
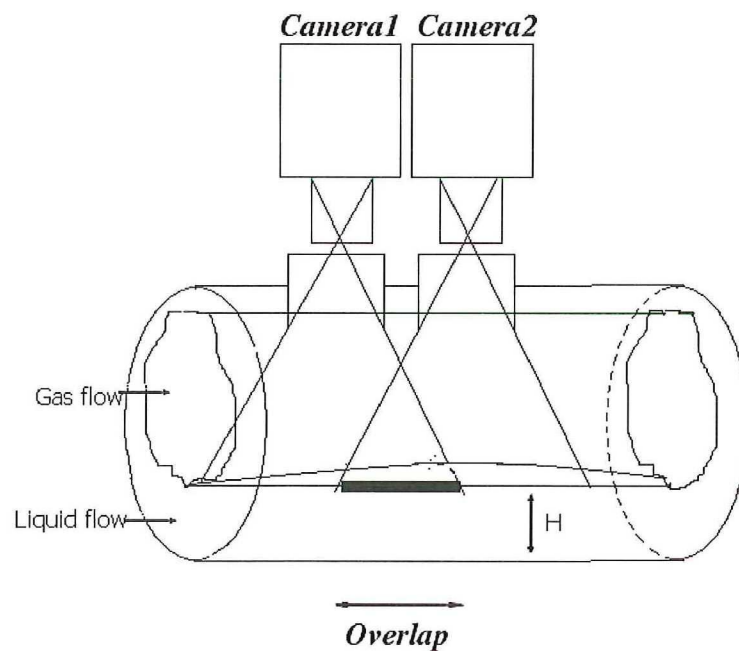
Figure B.2: Schematics of a possible setup for the use of stereophotography in annular flow. Two camera's are focused on the liquid layer in the annular flow, with an overlap of the pictures. The cameras should be triggered such that the pictures are taken at the exact same time.

Appendix C

Matlab routine

In this appendix, the matlab routine is shown with which the roll-wave frequency and velocity are determined.

```matlab
clear;

% constants
se0  = strel('disk', 2);
seD  = strel('disk',10);
se   = strel('disk',20);
P1 = 50;
P2 = 10000;
    Width = 600;
    Height = 400;
    XSTART = ((800 - Width)/2) -1 ;
    YSTART = ((600 - Height)/2)-1;
    rect = [XSTART YSTART Width Height];

% -- begin definition file-names
file_start =0;                              %first file
file_end = 4470;                            %last file

filename_01 = 'a40w60h0fr1000_';        %string with first part of filename
filename_02a = '000';
filename_02b = '00';
filename_02c = '0';
filename_02d = '';
filename_04 = '.jpg';                   %string with last part of filename
% -- einde definition file-names

%BEGIN LOOP OVER ALL FILES
for filenumber = file_start:(file_end)
    filenumber
        %Compose string with filename; strcat joins two strings
    filename_03=num2str(filenumber);
    if filenumber<10
      filename_02 = strcat(filename_02a,filename_03);
    elseif filenumber<100
      filename_02 = strcat(filename_02b,filename_03);
    elseif filenumber<1000
      filename_02 = strcat(filename_02c,filename_03);
    else
      filename_02 = strcat(filename_02d,filename_03);
    end
```

```matlab
        filename=strcat(filename_01,filename_02,filename_04);

    %Read in images for frequency
    A   = imread(filename);              %foto is a MxNx3 (color) matrix
    AA  = rgb2gray(A);                   %converting color image into grayvalue image, foto_gray
    AAA = imcrop(AA,rect);

    meanIM(filenumber-file_start+1)=mean(mean(AAA));

        %Read in images for velocity

    I = imadjust(AAA , [0 1],[1 0]);
    % background substraction=================================================
    background = imerode(AAA,se);
    I2 = imsubtract(I,background);

    level = graythresh(I2);              % transform the resulting picture in a bynar
    bw = im2bw(I2,level);

                                         % BW = BWAREAOPEN(BW,P) removes from a binar
    bw = bwareaopen(bw, P1);             % components (objects) that have fewer than

    BWsdil = imdilate(bw, se0);
    BWdfill = imfill(BWsdil, 'holes');

    BWfinal = imerode(BWdfill,seD);
    BWfinal = bwareaopen(BWfinal , P2);

    for j=1:numel(BWfinal(1,:))
        for i=1:numel(BWfinal(:,1))
            C(i,j)=BWfinal(numel(BWfinal(:,1))-i+1,j);
        end
    end

    for i=1:numel(C(:,1));
        for j=1:numel(C(1,:));
            if C(i,j)==1;
                C2(i,j)=0;
            else C2(i,j)=1;
            end
        end
    end

    C2 = bwareaopen(C2 , P2);
    for i=2:numel(C2(:,1))-1;
        for j=2:numel(C2(1,:))-1;
            if C2(i,j)==1 & (C2(i-1,j)==0 | C2(i+1,j)==0 | C2(i,j-1)==0 | C2(i,j+1)==0)
                XPosition(i) = i;
                YPosition(i) = j;
            end
        end
    end
    gemYPosition(filenumber-file_start+1) = mean(YPosition(2:numel(YPosition)));
    maxYPosition(filenumber-file_start+1) = max(YPosition(2:numel(YPosition)));
    minYPosition(filenumber-file_start+1) = min(YPosition(2:numel(YPosition)));
end

gem = mean(meanIM);
gem = gem*ones(1,numel(meanIM));
S   = std(meanIM);
gem2= gem+S/2;
```

```matlab
for i=1:numel(meanIM);
    if meanIM(i) < gem(i) - S;
        data(i) = meanIM(i);
    else data(i) = gem(i);
    end
end
%=Bepaling van grenzen van de roll waves=====================================
for i = 1:numel(data);
    if data(i) < gem(i);
        result(i) = 1;
    else result(i) = 0;
    end
end

index=0;
for i = 3:numel(result);
    if (result(i) > result(i-1)) & (result(i) > result(i-2)) & (result(i)>result(i-3));
        index = index+1;
    else index = index;
    end
end
index;                                          % Number of roll waves in sample
frequency = index/(((file_end-file_start)+1)/1000)   % Roll wave frequency


P = 0;
for i=9:numel(result)-10
    if (result(i) > result(i-1)) & (result(i) > result(i-2)) & (result(i)>result(i-3))
        P=P+1;
        Position(P) = i;

        Ygem = gemYPosition(i-10:i+10);
        Ymin = minYPosition(i-10:i+10);
        Ymax = maxYPosition(i-10:i+10);

        x=1:1:numel(Ymin);                      % vector x
        p=polyfit(x,Ymin,4);                    % 4th degree polynomial
        y=polyval(p,x);                         % vector of 4th degree polynomial

        pp = polyfit(x,Ygem,4);
        yy = polyval(pp,x);

%           figure(2),subplot(4,2,P), plot(x,Ygem,'r',x,yy,'b');
%           figure(1),subplot(4,2,P), plot(x,Ymin,'r',x,y,'b');


        g=0;
        for i=2:numel(y)-1;
            if y(i)<y(i-1) & y(i)<y(i+1)
                g=g+1;
                t_pos_a_min(g) = i;
                if g==1
                    t_a_min = i;
                elseif g==2
                    t_a_min  = t_pos_a_min(2);
                end
            end
        end
        T_a_min(P)=t_a_min;
```

```matlab
g=0;
for i=2:numel(y)-1;
    if y(i) > y(i-1) & y(i) > y(i+1)
        g=g+1;
        t_pos_b_min(g) = i;
        if g==1
            t_b_min = i;
        elseif g==2
            t_b_min = t_pos_b_min(1);
        end
    else t_b_min = 1;
    end
end

if t_b_min> t_a_min;
    t_b_min=1;
end

T_b_min(P) = t_b_min;


g=0;
for i=2:numel(yy)-1;
    if yy(i)<yy(i-1) & yy(i)<yy(i+1)
        g=g+1;
        t_pos_a_gem(g) = i;
        if g==1
            t_a_gem = i;
        elseif g==2
            t_a_gem = t_pos_a_gem(2);

        end
    else t_a_gem = yy(numel(yy));
    end
end
T_a_gem(P)=t_a_gem;

g=0;
for i=2:numel(yy)-1;
    if yy(i) > yy(i-1) & yy(i) > yy(i+1)
        g=g+1;
        t_pos_b_gem(g) = i;
        if g==1
            t_b_gem = i;
        elseif g==2
            t_b_gem = t_pos_b_gem(1);
        end
    end
end

if t_b_gem> t_a_gem;
    t_b_gem=1;
end

T_b_gem(P) = t_b_gem;

Δ_t_min = (t_a_min-t_b_min);
Δ_t_gem = (t_a_gem-t_b_gem);

Velocity_gem(P) = (Width*39.4*10^(-6))/(Δ_t_gem/1000);
```

```matlab
        Velocity_min(P) = (Width*39.4*10^(-6))/(Δ_t_min/1000);
    end
end
tijden = [T_b_min' T_b_gem' T_a_min' T_a_gem'];
Velocities = [Velocity_gem' Velocity_min'];

for i=1:numel(Velocity_gem)
    if  Velocity_gem(i) > 1.5 & Velocity_gem(i) < 4 & Velocity_min(i) > 1.5 & Velocity_min(i)
        Velocity(i) = (Velocity_gem(i) + Velocity_min(i))/2;
    elseif Velocity_gem(i) > 1.5 & Velocity_gem(i) < 4
        Velocity(i) = Velocity_gem(i);
    elseif Velocity_min(i) > 1.5 & Velocity_min(i) < 4
        Velocity(i) = Velocity_min(i);
    else Velocity(i) = 0;
    end
end
j=0;
for i=1:numel(Velocity)
    if Velocity(i) > 0
        j=j+1;
        finalvelocity(j) = Velocity(i);
        finalposition(j) = Position(i);
    end
end
VelPos = [finalvelocity' finalposition']
```